ORIGINAL ARTICLE



Seismic collapse analysis of unreinforced masonry buildings through applied element micro-modelling and crack width-based damage measures

Ciro Canditone¹ · Fulvio Parisi¹ · Dina F. D'Ayala² · Arianna Guardiola-Villora³

Received: 20 February 2025 / Accepted: 10 July 2025 / Published online: 21 July 2025 © The Author(s) 2025

Abstract

Unreinforced masonry (URM) structures subjected to moderate-to-severe earthquake ground motion often experience a poor performance, characterised by extensive cracking phenomena and the activation and development of collapse mechanisms. This produces high repair costs and a severe threat to human life. Furthermore, outward projection and accumulation of debris may reduce road serviceability, undermining rescue efforts and increasing post-event downtime. In this study, the suitability of the Applied Element Method – a discrete crack, rigid body and springs-based numerical technique – to capture damage spread, collapse mechanism activation and debris projection phenomena is tested against experimental data. Fracture energy-based softening laws are employed, improving numerical accuracy over the standard brittle failure models commonly implemented within AEM tools. The validated models are then used to assess the seismic performance of URM buildings under varying masonry quality, and hence mechanical properties. The study leverages on the inherent advantage of the AEM, that is, explicit simulation of cracking phenomena and body fragmentation with lower computational demand than other advanced numerical techniques, in order to: (i) simulate complex failure mechanisms, eventually leading up to collapse activation and subsequent stages of debris formation and accumulation; (ii) introduce novel damage measures that are able to explicitly quantify crack propagation and severity in URM load-bearing structures.

Keywords Applied element method · Unreinforced masonry structures · Seismic performance assessment · Damage assessment · Structural collapse

³ High Technical School of Architecture, Politechnic University of Valencia, Camino de Vera, Valencia 46022, Spain



[☐] Fulvio Parisi fulvio.parisi@unina.it

Department of Structures for Engineering and Architecture, University of Naples Federico II, Via Claudio 21, Naples 80125, Italy

Department of Civil, Environmental and Geomatic Engineering, University College London, Gower Street, London WC1E 6BT, UK

1 Introduction

Unreinforced masonry (URM) buildings subjected to moderate-to-severe earthquake loading conditions typically experience a poor performance, as observed during several seismic events such as the 2009 L'Aquila earthquake (Augenti and Parisi 2010; D'Ayala and Paganoni 2011). The occurrence of partial or complete structural collapses is a foremost cause of human life losses in earthquake scenarios, with fatalities being mainly caused by factors such as: (i) crushing or suffocation under collapsed structural elements; (ii) asphyxiation due to collapse-generated dust; (iii) delay in search and rescue operations (see, for instance, (Kuwata et al. 2005). Outward projection of debris is a major concern as well, because it may result into reduced road serviceability, potentially undermining rescue efforts and post-event recovery. On the other hand, extensive cracking phenomena, while not necessarily constituting a threat to residual vertical load-bearing capacity, may still significantly compromise building usability and make repair or retrofit interventions economically unfeasible. Such aspects may be quite hard to account for through standard tools typically used for structural assessment of URM buildings, such as Equivalent Frame modelling (EFM) or limit analysis (LA). While less computationally demanding than other structural modelling strategies, EFM, based on structural discretisation through deformable Timoshenko beams jointed with rigid end offsets that simulate spandrel-pier intersection zones, suffers from several drawbacks, critically highlighted in works such as (Quagliarini et al. 2017). These include: (i) difficulties in the modelling of highly irregular geometries, even in single walls with openings (see, e.g., (Parisi and Augenti 2013); (ii) the disregard of bond pattern effects; (iii) inability to account for actual crack patterns. On the other hand, while bond pattern effects can be implemented within limit analysis tools to analyse both out-of-plane and in-plane ultimate response (D'Ayala and Speranza 2003; D'Ayala 2005, 2013), their use is limited to the identification of the most likely collapse mechanism and associated load multiplier; crack width evaluation and post-failure phenomena remain, thus, unaddressed. Higher accuracy in these regards can be pursued through more advanced modelling techniques. According to the taxonomy established in (Lourenço 1996), these techniques fall within two broad categories: macro and micro-modelling approaches. Within macromodelling approaches (Fig. 1a) the mechanical response of all constituents - masonry units, joints and their contact interfaces – is lumped into that of one equivalent material; masonry

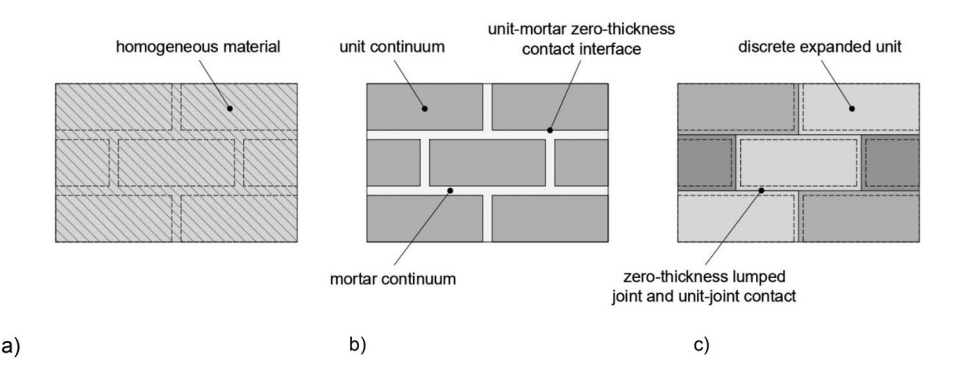


Fig. 1 Numerical modelling approaches for the simulation of URM: $\bf a$ macro-modelling $\bf b$ advanced micro-modelling $\bf c$ simplified micro-modelling



texture is disregarded, treating masonry as a homogeneous medium. This approach seems reasonably adequate in the case of masonry typologies such as adobe masonry, in which similar mechanical properties are found for both units and joints (Parisi et al. 2019; Canditone et al. 2023). When more remarkable discontinuities are found (e.g. strong unit-weak joint configurations, such as fired brick and lime mortar masonry), an accurate modelling of the masonry fabric (micro-modelling) may be more suitable, to capture bond pattern effects on damage onset and propagation. This may be pursued either through an advanced approach (see Fig. 1b), according to which all individual constituents are explicitly modelled and characterized, or through a simplified approach (see Fig. 1c), in which mortar and unit-joint interface behaviour is lumped into zero-thickness interfaces, and units expanded in size to accommodate mortar joint presence.

With regards to Finite Element Method (FEM), the incorporation of cracking effects within the numerical model is generally feasible only within a small strain and/or displacement range. While cracking can be simulated phenomenologically by means of smeared crack approaches, numerical instabilities may in fact occur in the large strain and/or displacement field due to excessively distorted meshes. Model remeshing could deal with such issues, albeit at substantial computational costs. Another technique lies in the use of zerothickness discontinuities, embedded within the continuum domain, to act as potential slip planes (so-called discrete crack approaches). However, to ensure nodal compatibility, FEM solvers must either (i) rely on complex algorithms to accommodate large strains/displacements within the original mesh, or (ii) generate new nodes along element slip and/or rotation paths. The latter calls for the reassembling of the global stiffness matrix, all the while leading to an increase in DOF number, substantially increasing computational burden. The simulation of heavily damaged structures undergoing fragmentation and impacts, as well as quantification of the extent and distribution of debris, remains thus a challenging task within a FEM framework (Grunwald et al. 2018).

Such limitations may be overcome through explicitly discontinuous formulations, such as the Discrete Element Method (DEM) or Applied Element Method (AEM). Both methods are based on the discretisation of a structure into a set of semi-independent discrete bodies; these interact with each other by means of contact points, automatically generated and distributed along contact interfaces. Forces, deformations and other interactions are calculated directly at a limited number of contact points, rather than along continuous contact surfaces. This enables DEM and AEM to bypass many of the numerical challenges associated with standard FEM in the large strain and/or displacement fields. The transition from a continuum into a discontinuous system, in fact, occurs by tracking finite displacements and rotations of discrete bodies, updating contact positions and checking conditions for separation and new contact generation as calculation progresses. This enables the simulation of crack propagation and post-failure collapse dynamics with lower computational burden, and greater accuracy, than continuum-based techniques. While originally developed within the field of rock and soil mechanics (Cundall 1971, 1988), DEM use has been expanded to URM analysis in works such as (Livesley 1992; Bui et al. 2017; Pulatsu et al. 2020, 2022), addressing computational efficiency, uncertainties, and spatial variability of material properties (Pulatsu et al. 2023a, b). On the other hand, AEM was initially formulated for linear elastic structural analysis (Meguro and Tagel-din 2000) and subsequently extended to nonlinear problems such as fracture propagation and buckling (Meguro and Tagel-din 1997, 1999). Works dealing with URM simulation by means of the AEM can be found in



(Malomo et al. 2019; Adhikari and D'Ayala 2020; Calò et al. 2021; Adhikari et al. 2023; Canditone and Parisi 2024). A comprehensive review on the use of discontinuum tools for URM seismic assessment can be found in (Malomo and Pulatsu 2024).

Based on the above discussion, the present study aims at expanding knowledge on and implementation of AEM simulation of URM structures under seismic actions, assessing the sensitivity of collapse configuration and capacity of URM buildings under varying masonry type, and hence its mechanical properties. While past research experience has showcased AEM suitability in capturing the complex damage progression and failure mechanism of URM elements, assemblies and buildings, fewer works have addressed its accuracy in simulating the dynamic behaviour of severely damaged structures and accurately reproduce collapse activation and subsequent dynamic evolution, including phenomena of debris projection and accumulation. Thorough validation of this numerical technique against available experimental data may significantly support future works aimed at simulating complex progressive collapse phenomena and predict extent and trajectories of structural debris. Furthermore, within the present work, explicit simulation of cracking phenomena through the AEM is employed to introduce novel damage measures (DMs) able to quantify (i) damage propagation, based on the occurrence of tensile and/or shear failures, in terms of cracked masonry volume percentages, and (ii) damage severity, based on residual crack displacements, within a repairability-based framework. By quantifying damage based on crack severity and propagation within the structural volume, these DMs provide a more nuanced assessment of structural degradation compared with traditional, displacement-based criteria. Furthermore, the use of such measures may not be limited to earthquake ground motion scenarios, allowing other loading conditions and tasks (including, e.g., vulnerability and fragility assessments) to be evaluated. This paper is thus organised as follows. Section 2 provides an overview of AEM formulation, along with a focus on the implementation of the adopted simplified micro-modelling approach within a commercially available AEM software package, Extreme Loading for Structures (ASI 2021). Section 3 then briefly focuses on the criteria which led to the selection of benchmark cases, and the rationale behind the analyses here performed. Sections 4 and 5 presents the results of nonlinear time history analyses, aimed at the simulation of shaking-table tests at wall assembly and building scales, respectively. In Sect. 6, validated models are then employed to predict seismic performance of non-engineered URM buildings, assessing their sensitivity to masonry type and associated mechanical properties. Structural performance is then discussed through novel Damage Measures, aimed at quantifying crack distribution, severity and potential repairability. Finally, Sect. 7 presents some concluding remarks.

2 Simplified micro-modelling of URM in an AEM framework

Within a simplified micro-modelling approach, masonry is represented as a set of discrete bodies, jointed through zero-thickness contact interfaces (Fig. 1c). Two different approaches can be employed to capture composite response, namely, an explicit and an implicit approach. Within explicit approaches, the behaviour of mortar and unit-joint interfaces is lumped into the interfaces between units; unit deformability and potential failure modes are then accounted for through either continuum mechanics or potential crack planes assigned to the units themselves, treated as sub-assemblies of rigid bodies. The explicit approach —



which was adopted in, for instance, (Pulatsu et al. 2020, 2022) – may produce high computational burden due to high DOF number. This may be unnecessary in weak joint-strong unit masonry types, the mechanical response of which is mainly controlled by joint behaviour; in such cases, an implicit, more expeditive approach may be pursued, treating units as non-deformable elements and assigning composite scale (i.e., macroscopic) properties to their contact interfaces. This approach – which enables capturing bond pattern effects on damage onset and propagation while limiting input data to masonry texture and composite scale properties – has been proven not to hinder accuracy, while reducing computational burden (Calò et al. 2021; Adhikari et al. 2023; Malomo and Pulatsu 2024). Indeed, the rigid body hypothesis significantly reduces computation time by limiting DOF number to the three translations, u_i , and three rotations, θ_i , of element centroids.

As strong unit-weak joint behaviour was observed in the two experimental studies considered herein (Magenes et al. 2010c; Candeias et al. 2017), an implicit approach was adopted. As per Fig. 2, two adjacent rigid units are assumed to be connected through an $m \times n$ grid of contact points, in which contact springs are automatically generated. Regarding contact point spacing, it should be noted that coarser spring discretisation does not hinder accuracy under axial loads, but may affect rotational stiffness; nonetheless, such errors become negligible if $m \times n > 10$ (Meguro and Tagel-din 2000). Within this work, the adopted contact point number per each contact plane is equal to 25. Assuming d as the distance between the two centroids, and the contact plane to be described by the units' height h and thickness t, the generic spring will thus account for the deformability of a finite volume δ_{v} , given by Eq. 1:

$$\delta_{\rm v} = d \cdot \delta_{\rm t} \cdot \delta_{\rm h} = d \cdot \left(\frac{t}{n}\right) \cdot \left(\frac{h}{m}\right)$$
 (1)

Normal (k_n) and tangential (k_s) stiffness values of a single spring can be taken according to Eqs. 2 and 3, based on masonry axial and tangential moduli (E and G), and the parameters defining δ_v :

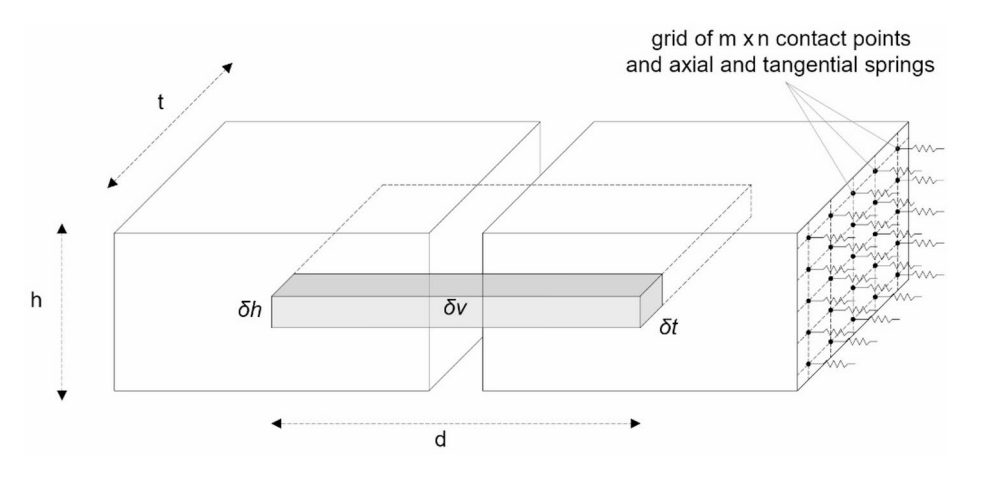


Fig. 2 Domain discretization within the AEM: element DOFs, contact point and spring distribution, finite volume δ_v accounted for by an individual spring



$$k_{\rm n} = \frac{E \cdot \delta_{\rm h} \cdot \delta_{\rm t}}{d} \tag{2}$$

$$k_{\rm s} = \frac{G \cdot \delta_{\rm h} \cdot \delta_{\rm t}}{d} \tag{3}$$

These stiffness values are then subsequently updated based on spring strains and the adopted constitutive models. Uniaxial material behaviour (Fig. 3a) was here described through parabolic hardening-softening functions in compression (Feenstra and De Borst 1996) and a linear elastic with linear softening law in tension. The Feenstra & De Borst compression model has already been used within discontinuum-based URM analysis – namely, via the so-called M-DEM (Macro-Distinct Element Method) – in works such as (Malomo and DeJong 2022). Within the referenced work, a piecewise, fracture energy-based multilinear compression stress -strain relationship was adopted. Within the present work, reference is instead made to the fully nonlinear, fracture energy-based parametric equations adopted, for instance, in the Finite Element software package DIANA (TNO DIANA 2009). These uniaxial curves serve as the backbone; all unloading and reloading paths, for instance due to load reversals, are, hence, bounded within such envelope. In both tension and compression, unloading is herein assumed to be bilinear, with a damaged unloading branch that is linear till zero stress followed by a horizontal branch till zero strain. The damaged unloading stiffness is taken as a function of peak masonry strain, in order to simulate the significant stiffness losses and strength degradation typically experienced by URM assemblies. On the other hand, reloading is linear with damaged secant stiffness corresponding to the last-reached point in either tension or compression. It should be noted that, within the AEM, compressive and tensile failure mechanisms are represented via inter-block penetration and interface opening/sliding, respectively.

Behaviour in shear, on the other hand, is assumed to be linear till the attainment of maximum shear strength, τ_{lim} , described through a Mohr-Coulomb formulation. Shear stress is, hence, considered a function of cohesion c, friction coefficient μ , and normal stress σ_{ν} , the latter here assumed to be positive in compression and negative in tension. Post-cracking shear stiffness is taken based on the initial ratio between E and G, and the damaged E value. While shear failure is assumed as brittle, post-peak behaviour in tension and compression is described here through tensile and compressive fracture energies, G^f and G^c , which are estimated according to equations proposed in (Lourenço 2009), based on material tensile (f_t)

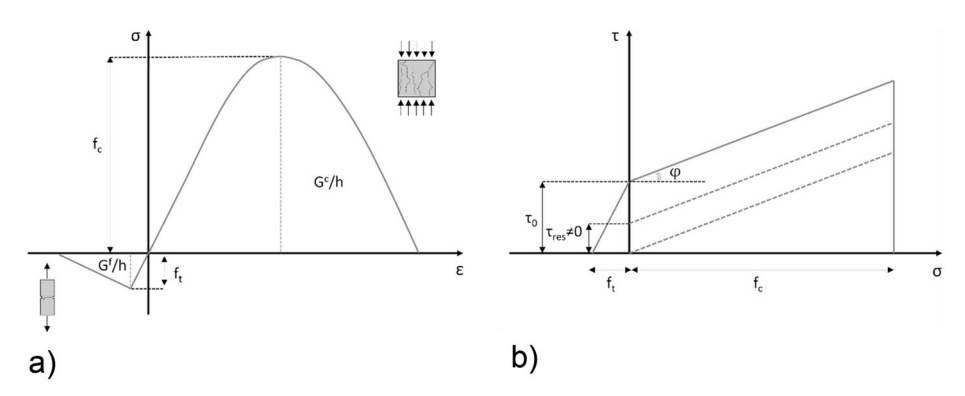


Fig. 3 Quasi-brittle uniaxial constitutive models (a) and adopted failure criterion (b)



and compressive (f_c) strength. To ensure mesh objective results, fracture energies were then divided by the cubic root of cuboid volume, assumed as characteristic length or crack bandwidth h. It should be noted that the use of fracture energy-based softening laws produces a significant improvement over the standard brittle failure models commonly employed in AEM applications (Malomo and Pulatsu 2024), as outlined in the following sections on discussion of analysis results. Failure envelope is described by means of a Mohr-Coulomb formulation with cut-offs in tension and compression, as shown in Fig. 3b. This criterion, the AEM-oriented mathematical formulation of which is described in further detail in (Malomo et al. 2018), enables accounting for brittle failures in tension-dominated states, sliding failure in shear-dominated states, and crushing failures in high compression states. The initial envelope is yielded by $c = \tau_0$, that is, cohesion equal to initial pure shear strength (i.e., under zero confining stress). If either shear strength τ_{lim} is reached or tensile/compressive strength is exceeded, material cracking occurs and cohesion drops to a residual value τ_{res} , which can be set to either zero (case of smooth cracks) or a fraction of the original value to simulate residual interlocking at course cracked surfaces (Van Der Plujm 1993; Augenti and Parisi 2011).

While spring strains in tension, compression and/or shear are reversible within the elastic stage, excursion into tensile or compressive inelastic stages and/or achievement of shear strength leads to discrete inelastic displacements. Springs thus enter a cracked state, that is, a state in which they may develop frictional residual shear strength and post-peak tensile strength that linearly decreases till zero between cracking strain, ε_{cr} , and ultimate tensile strain, ε_{tu} . Cracked springs are, meanwhile, still able to withstand compressive loads, potentially recovering crack displacements due to, for instance, load reversals. Both maximum and residual crack widths may then be directly computed via the numerical model. Springs may continue to deform at residual strength till the condition expressed in Eq. 4 is met:

$$\sqrt{\varepsilon^2 + \Upsilon_1 + \Upsilon_2} = \varepsilon_s \tag{4}$$

that is, when the norm of spring axial and tangential strains is found equal to a user-defined separation strain ε_s . While this value may be considered as a calibration parameter (Adhikari and D'Ayala 2020), it may be taken, for most quasi-brittle materials, as 0.10 (ASI 2021). If Eq. 4 is verified, the individual spring enters a separated state, so its stiffness is set to an almost null value to simulate significant stiffness loss. If all springs on a contact plane enter this separated state, bodies are free to slide due to reduced contact stiffness and eventually detach from and collide on each other.

3 Objectives and rationale for benchmark selection

As previously discussed, the main features of the AEM – i.e., rigid body and spring discretisation, efficient handling of nonlinear contacts, numerical stability under large strains and/or displacements, and ability to simulate cracking and fracture processes – make it particularly appealing for collapse analysis of quasi-brittle structural systems such as those made of masonry. The method may in fact be not only employed to simulate damage distribution and failure mechanism, but also post-collapse debris spatial distribution, which holds significant implications for emergency planning and structural retrofitting. However, thor-



ough numerical validation against experimental data, performed by matching key response parameters such as damage patterns and collapse modes, is needed to establish confidence in AEM results. To this end, two different benchmark case studies were selected. The first case study is a series of shaking-table tests carried out by (Candeias et al. 2017) on a C-shaped, brick masonry wall assembly, which was characterised by non-symmetrical openings' layout. The referenced study offers a detailed description of damage progression within the URM specimen, which incurred into the full development of an out-of-plane (OOP) failure mechanism, with subsequent debris projection. Thus, the simulation of this experimental benchmark first allows shedding further light onto AEM simulation of URM buildings that suffer OOP collapse, which is relatively unexplored within discontinuum-based analyses (Malomo and Pulatsu 2024) when compared with in-plane (IP) loading conditions. Furthermore, the simulation of that experimental tests assesses the AEM accuracy in correctly capturing the volume involved in the mechanism and debris trajectories. The reduced scale of the first case study does not however allow evaluating whether the AEM would correctly capture the interaction of URM walls with floor and roof systems, and how this may affect damage propagation at building scale. To this aim, a second benchmark was selected in (Magenes et al. 2010c). The specimen was also characterised by non-symmetrical openings' distribution, but it consisted of a two-storey full-scale building with timber floor and pitched timber roof. Even though no full collapse was observed, the second benchmark offers the possibility to assess AEM accuracy in capturing IP-OOP interaction, as well as damage distribution within a more complex structure, bridging the gap between assembly-scale and building-scale analyses.

4 Simulation of LNEC shaking-table tests on a brick masonry mock-up

4.1 Experimental benchmark description

The first benchmark consists of a series of shaking-table test that was performed on a brick masonry wall assembly at LNEC (Laboratório Nacional de Engenharia Civil, Lisbon, Portugal), as described in (Candeias et al. 2017). The work was aimed at the characterization of the OOP response of asymmetrical masonry assemblies up to complete collapse. To that aim, the testing protocol consisted of multiple tests under increasing shaking intensity, using a real ground motion recorded during the February 21, 2011, Christchurch (New Zealand) earthquake. Specimen walls were 235-mm-thick and rested over a 200-mm-thick reinforced concrete slab. Masonry was fabricated according to English bond pattern, using $235 \times 70 \times 115$ mm³ (length × height × thickness) clay bricks assembled through hydraulic lime mortar joints with thickness of 15–18 mm. Six wallets, $1000 \times 1000 \times 235$ mm³ (length × height × thickness) were likewise assembled. Three wallets were subjected to uniaxial compression tests to evaluate Young's Modulus *E* and compressive strength f_c of masonry, whereas the remaining specimens were tested under diagonal compression to evaluate tensile strength f_c Material properties and their coefficients of variation (CoVs) are summarised in Table 1.

The wall assembly specimen, having the plan view and elevation schematically represented in Fig. 4, was characterized by a 3.50 m long, 2.85 m tall façade (East wall), with a central 0.80×0.80 m² opening and gable end. The façade is connected to two 2.25×2.25



Table 1 Mechanical properties of brick masonry, adapted from (Candeias et al. 2017)

Statistics	ρ	Е	f_c	f_t	f_{cm}
	$[kg/m^3]$	[MPa]	[MPa]	[MPa]	[MPa]
Mean	1,890	5,170	2.48	0.10	2.00
CoV	3%	29%	14%	19%	-

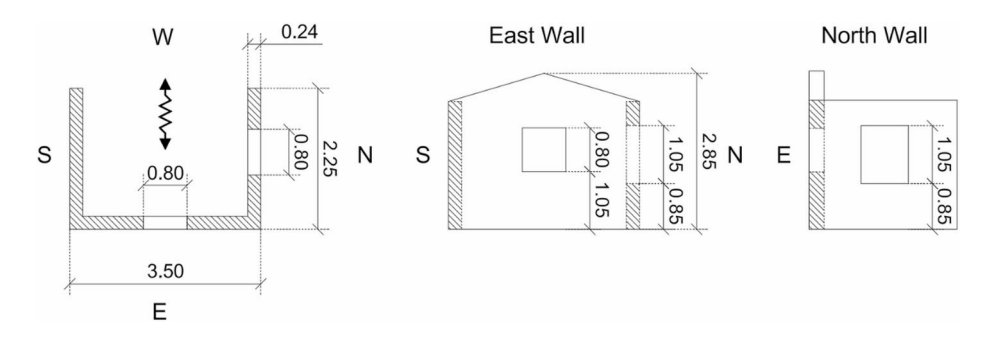


Fig. 4 Schematic representation of LNEC brick house specimen's geometry (dimensions in m)

m² return walls (length × height), one being solid (South wall) and the other (North wall) sporting a $0.80 \times 1.05 \text{ m}^2$ window opening. A complete description of the experimental setup and dynamic characterization, which is outside the scope of this paper, can be found in (Candeias et al. 2017). A frequency f=21.3 Hz was observed for Mode 3, which is associated with the OOP-dominated experimental response of the specimen when subjected to the planned E-W load protocol. The original ground motion record was applied 8 times on the E-W axis, scaling the signal up to 300% to increase intensity. Although good agreement between reference and shaking-table signal was obtained with regards to displacements, the latter reached higher PGA values than intended (maximum PGA=1.27g, 50% larger than the target). The specimen developed an approximately linear elastic response during the first four tests, that is, below PGA=0.40g. Moderate cracking – less than 1 mm in width – was observed after Test 05 (0.51g) near openings corner and later spread both in the North return wall and façade during Test 06 (PGA=0.78g). As these cracks further developed, sub-horizontal cracks also formed at the base of the IP loaded piers of the return wall and the OOP loaded NE corner pier, due to torsional effects. All cracking occurred in mortar joints, with no significant damage being observed into masonry units. Collapse took place during Test 08 (PGA=1.27g) and its sequence can be described as follows according to (Candeias et al. 2017): (i) out-of-plane overturning of a large portion of the gable, which fell eastward; (ii) rocking and rotation of the NE pier at specimen's front, with the NW pier subjected to simple rocking; (iii) development of a three-body mechanism for the IP loaded piers and spandrel, leading to loss of lintel stability and separation between those elements; (iv) backward fall of NW pier, and of the spandrel above, both falling down out of the shaking table; and (v) OOP failure of the remaining gable portion. The NE corner pier, which suffered relevant rocking and rotation, remained into an unstable equilibrium condition.



4.2 AE model description

As only limited instances of unit cracking were observed in the tests, a choice was made to disregard potential failure surfaces within the units and represent the specimen's English bond pattern by means of 1,734 8-node rigid elements, each accounting for an individual unit (see Fig. 5). All nonlinearities were lumped into unit-unit interfaces, which were assigned material properties according to experimental data in (Candeias et al. 2017). Tensile strength and cohesion were taken as the average experimental value $(f_t = c = 0.10 \text{ MPa})$, which was characterised by means of diagonal compression tests. Only Young's modulus E had to be calibrated. As observed in other numerical works dealing with the same benchmark (Silva et al. 2020; Kita et al. 2020; Khattak et al. 2023), calibration of E was needed to improve the numerical-experimental agreement in terms of both elastic displacements and natural frequencies, leading to the adoption of the lower experimental bound (E=3.671 MPa). Timber lintels were modelled by means of 40 8-node rigid elements, with mechanical properties (E=10,000 MPa, G=3,846 MPa, $\rho=590 \text{ kg/m}^3$) inferred from literature data. The shaking table was modelled by means of a 0.20 m thick 8-node element, and elastic mortar properties were assigned at specimen-slab interface because no sliding was experimentally observed. A total of 10,650 DOFs was considered.

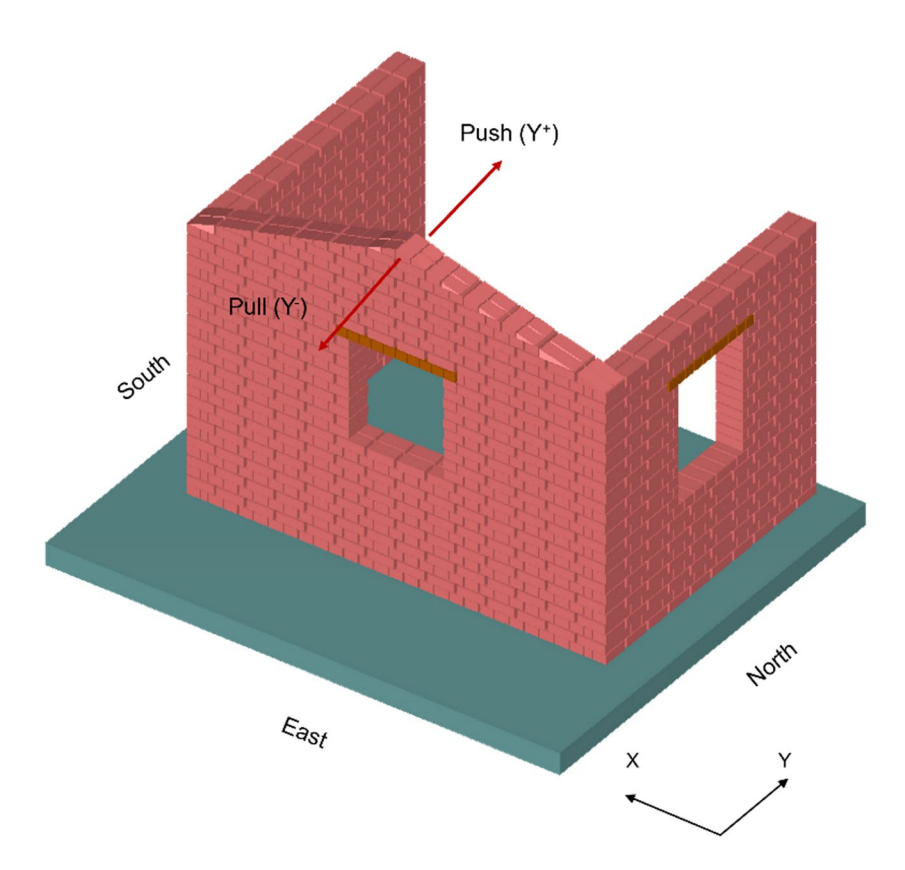


Fig. 5 AE model for the LNEC brick masonry mock-up



4.3 AE analysis results

This section deals with numerical results from both linear and nonlinear, static and dynamic analyses. Eigenvalue analyses were first run to check whether experimental modal behaviour could be captured and to calibrate masonry stiffness accordingly. It was found that, to correctly capture the specimen's natural OOP mode (Mode 3) in terms of frequency, Young's modulus value had to be reduced to 1,364 MPa, reaching a numerical-experimental deviation $\Delta f = -8\%$. This was also observed in the paper by (Khattak et al. 2023), who made use of the same modelling technique. However, such a lower value of Young's modulus was later observed to overestimate the elastic displacements yielded by nonlinear time history analysis (NLTHAs) by up to 50%. Thus, E=3,671 MPa (lower experimental bound) was found to be a trade-off value, which yielded 15% error on elastic Peak Roof Displacement (PRD), measured at gable top, and 40% error in the initial frequency, an admittedly large error which was deemed acceptable to get a more accurate displacement response. Nonlinear static analyses (NLSAs) were then run to assess the numerical model's base shear capacity and compare it with experimental failure PGA. A maximum numerical base shear coefficient $\alpha_u = 1.17g$ was found, which is 8% lower than its experimental counterpart. Experimental failure patterns, namely, flexural cracks at NE corner pier base and gable base cracks, were captured. Notably, some unrecorded mechanisms emerged, such as tensile failure at the return wall interface under outward loading (EW, Y⁻) loading and a sub-vertical crack within the gable centre under inward (EW, Y⁺) loading, as observed also previous numerical studies addressing the same benchmark (Kita et al. 2020; Khattak et al. 2023). NLTHAs were then performed, to check whether dynamic behaviour, damage progression and collapse mechanism could be captured. As the first four shaking-table runs were met with a linear elastic response, a choice was made to simulate acceleration time histories starting from this seemingly undamaged condition. Experimental ground motion retrieved from shaking-table response were used as input acceleration time history for the numerical model, simulating Test 04 to Test 08. This allowed to remove filtering effects of the shaking-table system. Average ground motion duration was 21.9 s; a timestep $\Delta t = 0.005$ s was adopted, with 5 step subdivisions, resulting into a total of 114,575 steps. Analyses were run using a 16 GB RAM, AMD Ryzen 7 4700U (2 GHz) processor-equipped machine and took approximately 5 h. Numerical-experimental comparison in terms of response displacement time-histories at gable top is shown in Fig. 6 for selected test runs. The overall trend is captured for both quasi elastic behaviour (Fig. 6a, Test 4, PGA=0.40g) and highly inelastic behaviour (Fig. 6b, Test 7, PGA=0.84g). For instance, both positive and negative peaks of Test 4 are captured with about 4% error. Similar errors were met with regards to Test 7, the positive and negative peak displacements of which were captured with about -3% and +8%errors, respectively. Lower agreement was found for Test 8 (Fig. 6c, PGA=1.27g). While the first negative peak was captured, this was not the case for later positive oscillations, which were underestimated. While past research experience (De Jong 2009) has shown rocking impacts to be best reproduced through stiffness-proportional damping schemes, it should be noted that the AEM makes use of a zero-damping scheme. Thus, energy dissipation only occurs through joint failures (hysteretic damping) and impacts (physical damping). Discrepancies in the latest analysis stages may be thus motivated, on one hand, by the numerical simulation of damage mechanics (here influenced both by fracture energies as well as



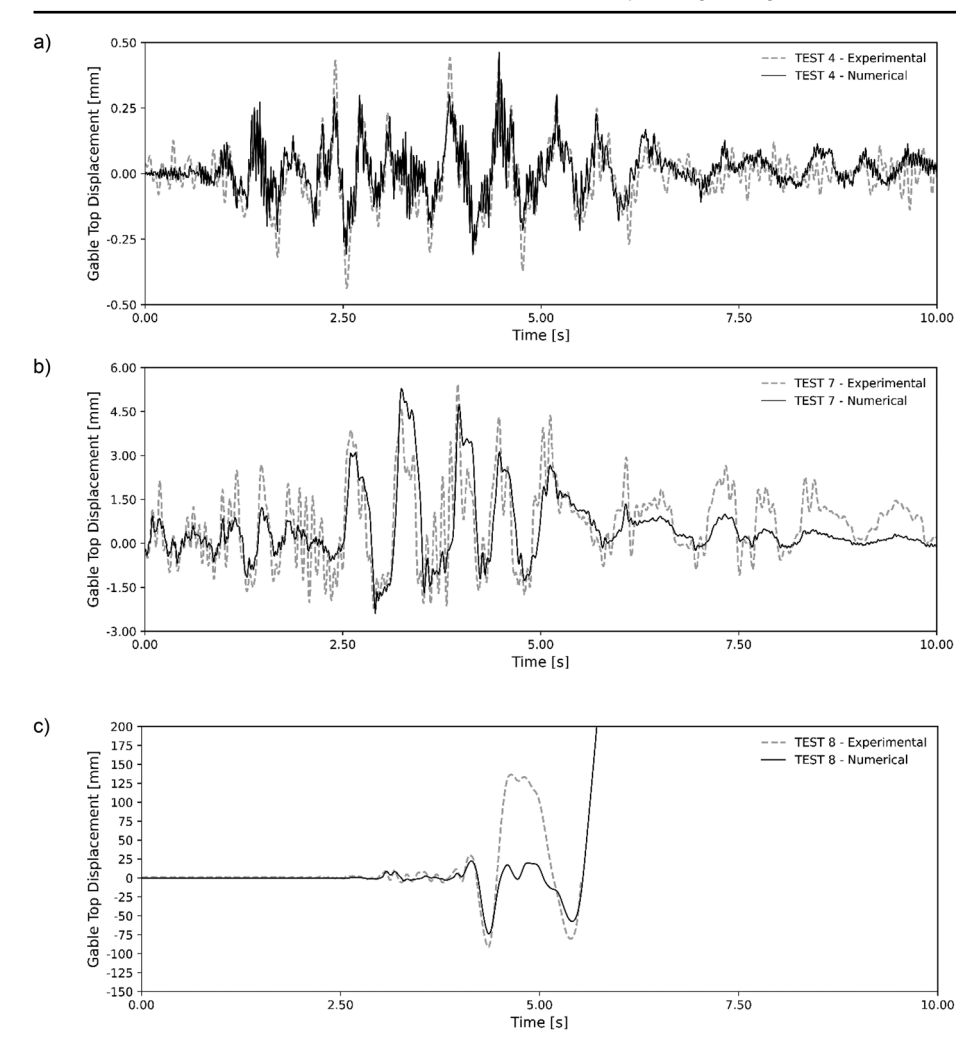


Fig. 6 Numerical and experimental displacement time histories for a test 4, b test 7, c test 8

the definition of a separation strain ε_s), and on the other, by numerical handling of rocking impacts through the coefficients of restitution and post-separation contact stiffnesses.

With regards to damage progression, onset of numerical cracking occurred at openings corner under 0.40g, as observed during experimental tests. Both IP and OOP damage subsequently spread towards the corners during Tests 5 and 6 (0.51g and 0.78g PGAs). Crack width progression was also checked by monitoring crack displacements; crack widths lower than 1 mm were observed till Test 7, in agreement with experimental records. This threshold was eventually overcome, leading to full crack development, by Test 7 (PGA=0.84g), again in good agreement with the experimental crack pattern, eventually evolving into a collapse mechanism for PGA=1.27g. The resulting collapse mechanism, which developed during Test 8, was close to experimental results (see Fig. 7). The development of the simulated collapse mechanism (Fig. 7) could be described as follows: (i) first, OOP gable overturning



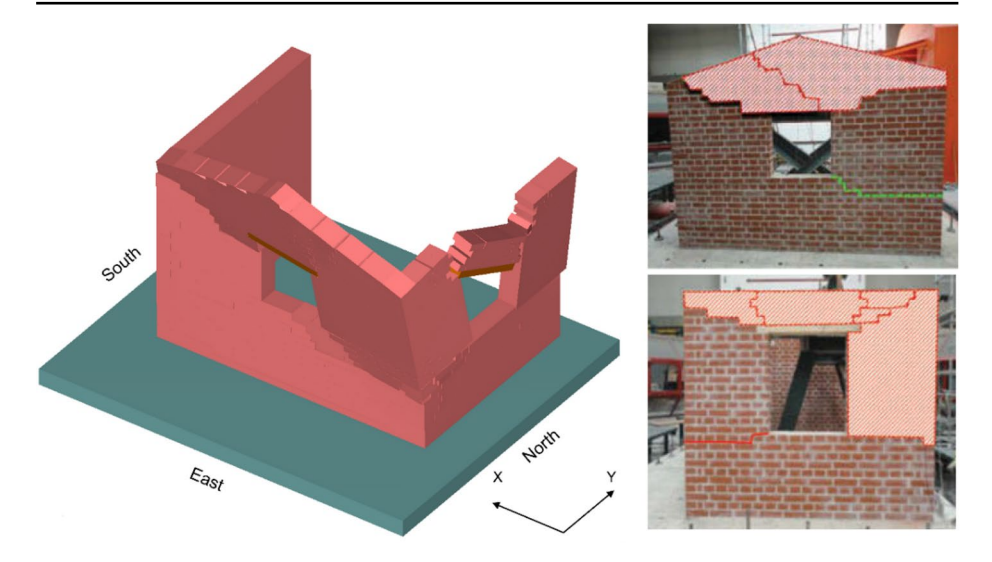


Fig. 7 Comparison between numerical collapse mechanism and damaged configuration after Test 8, adapted from (Candeias et al. 2017)

was observed; (ii) a sub-vertical crack within the gable acted as a hinge, allowing a small relative rotation between the two gable portions; (iii) relative rotation between the two gable portions also led to NE corner rocking and rotating, simultaneously with the development of the IP three-body kinematic within the return N wall. The trajectories of wall debris were found to be matching with experimental data, with the NW pier falling backwards and the gable overturning eastwards, both out of the shaking table. Post-processing of AEM results according to elements' volume and coordinates yielded an estimate of the total volume involved in the numerical failure mechanism, which was found approximately equal to 1.57 m³; an analytical estimate of its experimental counterpart, based on the analysis of the crack pattern in Fig. 7, yielded a value of approximately 1.50 m³.

It should be noted that, in (Candeias et al. 2017), the gable did not develop a sub-vertical crack, but rather a symmetrical base crack; the NE pier, therefore, did not interact with the gable during its collapse, and thus managed to remain in a precarious equilibrium position till the end of the test. It should be noted, however, that such failure mechanisms are more strongly associated with the absence of torsional irregularities; see, e.g., (D'Ayala et al. 2019). On the other hand, an irregular layout of openings is often associated with a nonuniform load distribution, and hence, an asymmetric failure mechanism (Parisi and Augenti 2013). This was, in fact, observed in other numerical studies dealing with the same specimen, such as (Al-Shawa et al. 2017; Chácara et al. 2017, 2018; Silva et al. 2020). Thus, the actual failure mechanism may have resulted from the presence of local vulnerabilities associated with, for instance, spatial scatter in material properties, which was not considered here. To this end, spatial stochastic analyses, such as those developed in (Pulatsu et al. 2022, 2023b), may be considered. Despite these shortcomings, it should be mentioned that the present work captured displacement time-histories with an accuracy degree comparable to (Al-Shawa et al. 2017; Chácara et al. 2018; Silva et al. 2020), which employed FEM micro-modelling, FEM macro-modelling and distinct macro-elements (M-DEM), respectively. Furthermore,



displacement trends were captured with higher accuracy than (Malomo and DeJong 2022; Khattak et al. 2023), both of which used discontinuum methods and underpredicted displacement peaks for Test 7. With regards to damage pattern and failure mechanism, the present work achieved comparable accuracy with other numerical works, such as (Al-Shawa et al. 2017; Chácara et al. 2017, 2018; Silva et al. 2020), which also obtained a gable crack pattern characterized by an asymmetric damage at gable base and the formation of a sub-vertical crack. However, in this study, the AEM simulation is also able to track dynamic collapse evolution and debris projection, which could not be observed in the other works due to the employed numerical formulations (i.e., distinct macro-elements, FEM micro-modelling, FEM macro-modelling) being numerically unstable under large displacements. Finally, the present study also achieved greater accuracy compared to (Khattak et al. 2023), who also employed AEM. Similarly to the present study, (Khattak et al. 2023) successfully captured the IP three-body pier-spandrel kinematics; interestingly, it also captured the development of the previously mentioned sub-vertical hinge within the gable, highlighting the effects played by torsional irregularities over the crack pattern and failure mechanism. Despite significant OOP deflection, however, the gable and front pier themselves were not involved in the numerical collapse mechanism. As a similar accuracy degree was, supposedly, pursued with regards to specimen geometry, masonry block pattern, boundary and loading conditions, it is the authors' opinion that differences between the two AEM outcomes may rather be associated with material properties and constitutive behaviour. Differences may in fact be motivated by the adoption, in (Khattak et al. 2023), of higher-than-experimental tensile strength and cohesion values, to compensate for the use of brittle tensile and shear failure models. By doing so, authors may over-strengthened the model, hence underestimating damage spread and displacement peaks in the latest test runs – both of which appear to have been more suitably captured using fracture energy-based softening laws.

5 Simulation of EUCENTRE shaking-table test on a two-storey stone masonry building

5.1 Experimental benchmark description

A second, more complex experimental benchmark was selected to assess AEM suitability in reproducing the experimentally observed near-collapse behaviour of URM buildings, which was influenced by the complex interactions between IP and OOP loads as well as the role of deformable diaphragms over structural response. To this aim, shaking-table tests performed at the EUCENTRE laboratories (Pavia, Italy) were taken as benchmark (Magenes et al. 2010c, 2013). Three full-scale, non-symmetrical, two-storey, stone masonry buildings were tested under increasing severity of earthquake ground motion to investigate the effects of timber floor/roof stiffening and wall connection improvement on seismic response. This study focuses on the numerical simulation of seismic response of building specimen #1, which was characterised by a $5.80 \times 4.40 \text{ m}^2$ rectangular plan and flexible timber floor and roof systems. Approximately 320 mm thick walls were built; two outer leaves were assembled through approximately prismatic 100-to-150-mm-wide and 200- to-300-mm-long stones, which were connected to each other via pre-mixed hydraulic lime mortar joints. Smaller stones and mortar were employed to fill in the irregularities



Table 2	Mechanical	properties
of maso	onry	

Statistics	Е	G	f_c	f_t	γ
	[MPa]	[MPa]	[MPa]	[MPa]	[kN/m ³]
Mean	2,550	840	3.28	0.137	22.5
CoV	13.5%	14.8%	8%	21.8%	-

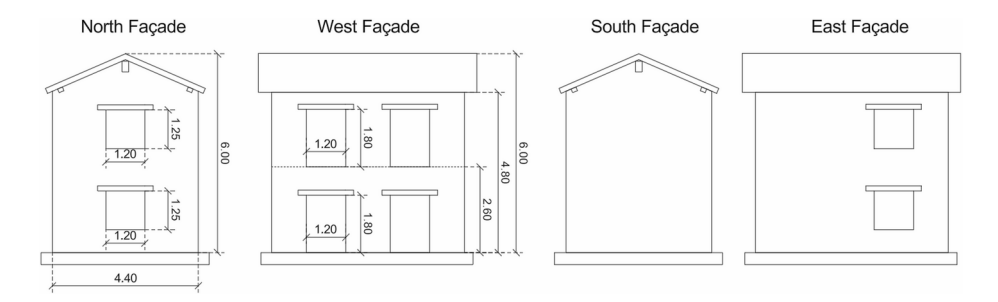


Fig. 8 Schematic representation of EUCENTRE stone house specimen geometry (dimensions in m)

between the two leaves, and good masonry interlocking achieved using passing-through stones. Indeed, no debonding phenomena occurred at prism, pier or wall scale (Magenes et al. 2010a, b, c). Passing-through stones were also employed at building corners and in the proximity of openings. Experimentally evaluated masonry mechanical properties and CoVs are summarised in Table 2 according to (Magenes et al. 2010a, b). The openings layout in Fig. 8 was purposefully designed as asymmetric to increase torsional behaviour, thus amplifying non-uniform demand on walls due to diaphragm load distribution. The two 5.80-m-long longitudinal walls were characterized by a different number and size of openings: the East wall had two 1.20 × 1.80 m² door openings per storey, whereas the West wall had only one 1.20 × 1.25m² window opening per storey. The same number, distribution and size of openings also characterised the North façade; by contrast, the South façade was solid. The two facades, about 6.00-m-tall, were characterised by gables due to the presence of an approximately 37° inclined pitched roof. The roof was assembled through a set of rafters, simply supported on a ridge beam and two spreader beams resting on top of the longitudinal walls. Planking was then nailed on top of the rafters. Similarly, the floor was built through joists, simply supported by longitudinal walls, and planks nailed on top. Additional 3.2 tons masses were added over the floor by means of laminated rubber blocks; clay tiles, each weighing about 3 kg, were instead nailed on top of the roof planks. The total weight of the specimen is estimated in 679 kN, as a result of the following components: 616 kN for the approximately 27 m³ URM walls; 8.6 kN for the floor structure; 11 kN for the roof structure; 43.7 kN for additional masses, including the roof tiles. Further details on the specimen may be found in (Magenes et al. 2010c, 2013; Guerrini et al. 2021).

A set of accelerometers was installed to monitor a total of 43 DOFs, complemented by a system of HD cameras which recorded the displacements of passive markers fixed on the longitudinal (East and West) walls. The specimen's natural vibration period was found to be T=0.13s (f=7.35 Hz) and was associated with OOP gable movements. The specimen was tested in the longitudinal (N-S) direction under five acceleration records based on the April 15, 1979, Montenegro earthquake (Ulcinj-Hotel Albatros station), generating OOP displacement of the gable façades. Specimen damage progression is detailed in (Kouris



et al. 2019). Spandrel cracking was detected during Tests 01–03 (0.07g to 0.32g PGAs), particularly in spandrels at the lower storey and at the ends of upper-storey spandrels. During Test 04 (PGA=0.51g), the IP and OOP cracking developed to a greater extent: spandrel cracks increased in width at both storeys, and severe OOP cracking of the façades also developed. Base gable cracks were observed. A further test with a PGA=0.63g led to the activation of the failure mechanism, which was characterized by slight overturning of the two gables – connected by means of the ridge beams – and IP mechanisms for piers and spandrels. Testing was temporarily stopped to install tie-rods and to check structural performance in a retrofitted configuration; subsequent results were not simulated within this study, so they are not discussed below.

5.2 AE model description

The specimen considered in this study was also a subject of previous numerical investigations based on EFM (Tomić et al. 2021) inverse engineering in a FE framework (Kouris et al. 2022), and rigid multi-body dynamics (Costa et al. 2015). An AEM model of a subassemblage, coinciding with the elements involved in the collapse mechanism, was also developed in (Morandini 2022). In (Tomić et al. 2021), masonry walls were discretised into piers, spandrels and rigid joints according to EFM principles; notably, the employed macro-element formulation accounted for OOP behaviour, which is not typically addressed in EFM. Diaphragm IP stiffness was accounted for by means of a linear elastic orthotropic membrane with an equivalent shear stiffness value G_{eq} taken according to (FEMA 356 2000) formulations. In (Kouris et al. 2019), masonry walls were modelled by means of deformable 8-node solid elements, with two-node beam elements and four-node shell elements being used to simulate beams and planks, respectively. Nonetheless, that study was aimed at capturing the experimental modal evolution described in (Kouris et al. 2019) through model updating, so it did not delve into advanced fracture and damage simulation. In (Costa et al. 2015), a system of rigid macro-blocks and nonlinear interfaces was developed according to the experimental crack pattern and subjected to the last experimental shaking-table record (PGA=0.63g). The AEM model developed in (Morandini 2022) was, similarly, aimed at capturing the activation of the collapse mechanism under PGA=0.40g. Interestingly, the numerical model included damage originated in previous test runs (PGA 0.05g to 0.30g) by reducing tensile strength and cohesion along crack edges. However, the model only included structural portions involved in the overturning mechanism, that is, the roof, the upper part of the South façade, the gable and second storey spandrels of the longitudinal façade. Therefore, the present study is the first attempt to capture the complex experimental response of the selected building specimen via an advanced, full-scale discontinuous numerical model (see Fig. 9). Admittedly, the mechanical response of URM elements and structures is known to be strongly influenced by masonry bond pattern; see, e.g., the discussion in (Szabò et al. 2023). Thus, an inaccurate modelling of URM bond pattern may significantly affect numerical accuracy. This recently motivated some researchers to explore the possibility of automatic or semi-automatic generation of high-fidelity discontinuous models, based on image processing (e.g., Milani et al. 2013; Griesbach et al. 2024). However, due to the lack of high-quality vision data, a choice was here made to simulate the slightly irregularly coursed masonry texture of the specimen by means of regular 8-node rigid elements (200 × 125 × 320 mm³ in size). Preliminary analyses were first carried out



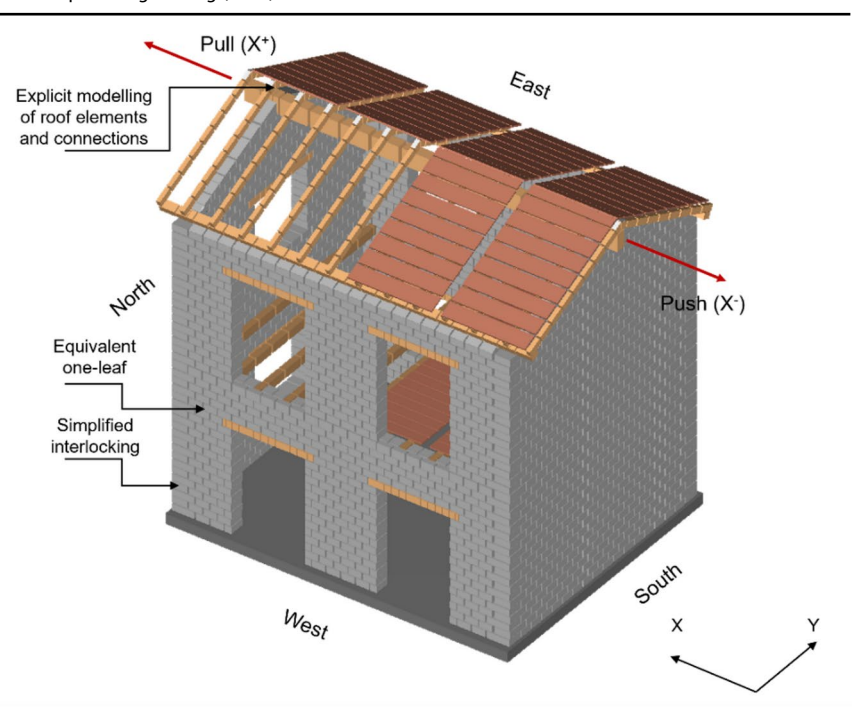


Fig. 9 AE model developed for the EUCENTRE full-scale specimen

at pier scale, benchmarking the numerical model against experimental results described in (Magenes et al. 2010b), hence showcasing the suitability of this approach. Given that the walls developed monolithic behaviour, no cross-sectional meshing was adopted, significantly reducing computational burden. Corner interlocking was simulated by means of 125 × 350 × 320 mm³ elements, arranged in a staggered pattern along the vertical axis. Timber lintels and the structural members of both the floor and roof systems were explicitly modelled according to their actual spacing and size; planking was also considered by means of an idealised discretisation. Increased density was assigned to plank elements to account for distributed additional masses. Such detailed modelling of the diaphragms was pursued as the interaction between timber members and masonry elements had been proven, both experimentally and numerically, to significantly influence both damage propagation and gable displacement capacity (Tomassetti et al. 2019; Calò et al. 2021). This detailed modelling of the building specimen resulted into 3,463 rigid elements with 20,778 DOFs. This derived from modelling of 2,634 stone units (including 148 corner units), 128 elements for timber lintels, 176 elements for floor joists, 100 elements for floor timber boards, 340 elements for roof structural members, and 85 elements for roof planking.

The masonry behaviour in tension, shear and compression was modelled following the approach discussed in Sect. 2.2. After some preliminary simulations, experimentally based strength values were complemented with stiffness properties for roughly dressed stone masonry listed in the Italian Building Code (D.M. 17.01.2018, Circolare n°7, 21.01.2019) to match dynamic properties. The timber material behaviour was described by means of nonlinear quasi-brittle constitutive models, following a study by (Khorsandnia and Crews 2015).



The timber tensile strength, compressive strength, Young's and shear moduli were assigned values taken from the Italian Building Code (D.M. 17.01.2018, Circolare n°7, 21.01.2019) for D24 timber class. This was inferred from average timber density, calculated according to total weights given in (Guerrini et al. 2021). Planks were assigned an equivalent shear stiffness G_{eq} , which was based on values for single-sheathing boards simply nailed on top of joists (FEMA 356 2000). It is noted that such a value matches those used in (Costa et al. 2015; Tomić et al. 2021; Kouris et al. 2022). To avoid any unrealistic stress transfer between the diaphragm and load-bearing walls, a gap was introduced between planking and masonry. Due to the lack of information concerning the nailed connections, some assumptions had to be made with regards to nails number, diameter and positioning. The nail stiffness k_{ser} was taken according to Eurocode 5 (EC5 2004) by considering couplets of 3 mm diameter nails, whereas experimental values of yielding load $F_{\rm v}$ and peak load $F_{\rm max}$ were assumed according to (Dolan 1992). Finally, given the uncertainty about nail distribution and spacing, a simplified approach based on distributed equivalent springs was implemented, converting nail load-displacement relationship into equivalent stress-strain relationships. The material properties applied to the calibrated numerical model are summarised in Table 3, in which values derived from the referenced experimental works (Magenes et al. 2010a, b, c, 2013) are marked with *.

5.3 AE analysis results

A first set of analyses was carried out at pier scale to calibrate masonry material properties. Experimental results described in (Magenes et al. 2010b) were taken as reference, as the tested piers were assembled using the same materials and bond pattern of the full-scale building. The experimental behaviour of specimen CT02 was taken as a benchmark, due to the availability of applied load protocol, backbone curve, and damage propagation data. The specimen was $2.5 \times 2.5 \times 0.32$ m³ in size (length × height × thickness) and was first subjected to 0.20 MPa pressure. Axial loads were then kept constant in the later testing phase, during which the cantilevered specimen was subjected to cyclic displacements with increasing magnitude on top, reaching a peak load and maximum displacement respectively equal to 154 kN and 15 mm (corresponding to 0.6% horizontal drift). The same boundary conditions were implemented within the numerical model of the pier, where masonry was discretised through 8-node rigid elements $(200 \times 125 \times 320 \text{ mm}^3 \text{ in size})$. Both the numerical and physical specimens experienced diagonal shear failure; a comparison between the experimental response, here shown in terms of envelope curve, and the simulated cyclic response can be observed in Fig. 10a. While no calibration was needed with regards to strength and inelastic parameters, elastic properties had to be decreased by about 40% to capture initial lateral stiffness. Such considerable reduction could be justified by over-stiffening effects which may occur within discontinuum-based numerical approaches such as AEM, which are well documented in the literature on the topic (Malomo and Pulatsu 2024). It is worth pointing

Table 3 Mechanical properties employed within the numerical model

Material/component	ρ	Е	G	f_c	$f_t = c$	μ
	[kg/m ³]	[MPa]	[MPa]	[MPa]	[MPa]	[-]
Unreinforced masonry	2,207*	1,500	500	3.28*	0.137*	0.57
D24 Timber	590*	10,000	700	21	14	0.40
Planks	590*	7,000	12	16	7.2	0.40



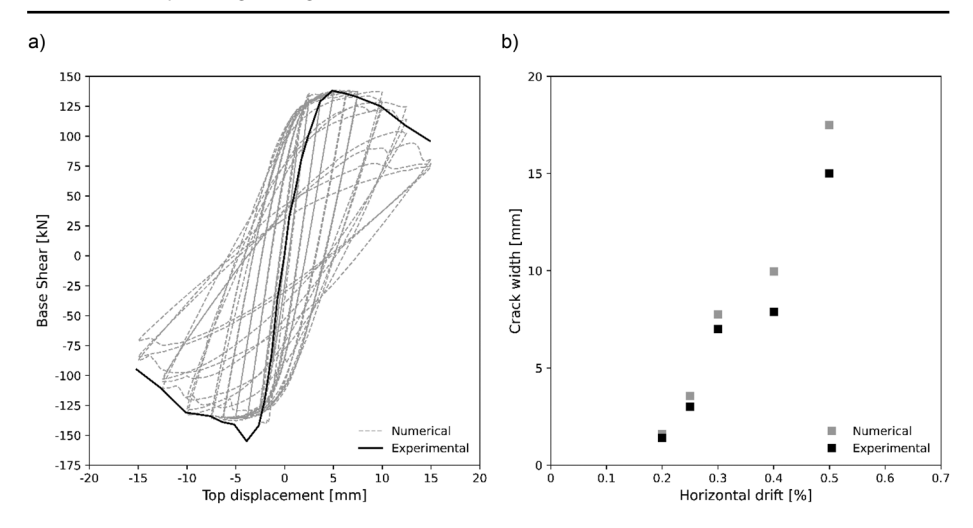


Fig. 10 Comparison between experimental and numerical data with regards to: a load-displacement response and b relationship between horizontal drift and crack width

out that the calibrated values of E and G fit well with those recommended in the Italian Building Code (D.M. 17.01.2018, Circolare n°7, 21.01.2019) for this masonry typology. A further comparison can be drawn with regards to crack widths; indeed, residual crack width values along the diagonals were measured in (Magenes et al. 2010b) at the end of each loading phase. As can be seen from Fig. 10b, the average numerical values approximate their experimental counterparts with maximum errors in the 20% range, generally overestimating them.

Based on such preliminary results, building scale analyses were then performed. The full-scale model accuracy was first evaluated in terms of total mass, achieving a 3.7% difference to the analytical estimate. Then, eigenvalue analyses were run to match the experimental dynamic behaviour by calibrating masonry stiffness accordingly. Both experimental and numerical first modes of vibration point to significant OOP gable top displacements, coupled with significant diaphragm distortions. However, a 23% overestimate of natural frequency was found when using experimental masonry stiffness properties; error margin dropped to 3% when adopting the values calibrated at pier scale, which yielded a natural frequency of 7.61 Hz. It should be noted that stiffness values similar to those adopted here (E=1,500 MPa, G=500 MPa) were also used in the numerical sub-assemblage AEM model validated in (Morandini 2022), who adopted E=1,130 MPa and G=395 MPa. The model was then subjected to the experimental shaking-table records. As the sampling frequency of the instrumentation was 960 Hz, time step was set to $\Delta t = 1/960$ Hz=0.001s, resulting in a total of 120,000 steps to simulate the five 25-s-long records. Analyses were run using a 16 GB RAM, AMD Ryzen 7 4700U (2 GHz) processor-equipped machine and took about 9 h. An overall fair agreement in displacement trend and peak response values was found both for intermediate (Fig. 11a, Test 3, PGA=0.31g) and high (Fig. 11b, Test 5, PGA=0.63g) acceleration values. Test 5 inelastic PRD in near-collapse conditions was captured with 4% error. A deviation between experimental and numerical results was observed in terms of residual displacements, due to a circa 5 mm permanent sliding of the spandrels and supporting lintels within the numerical model, which can be observed in Fig. 10b from circa 15 s



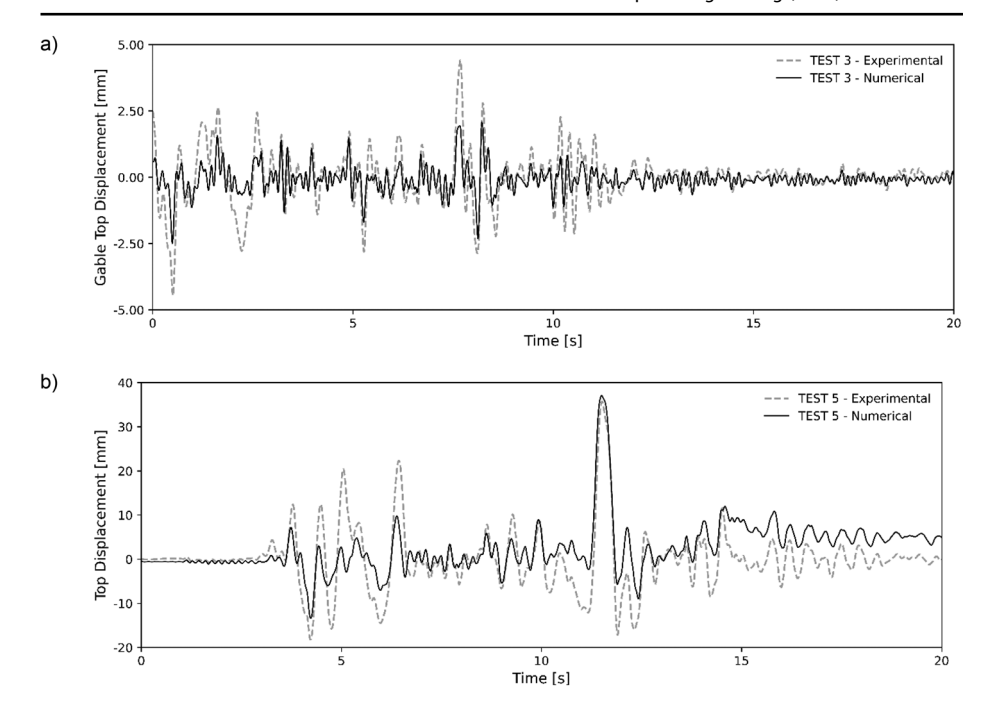
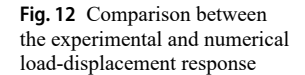
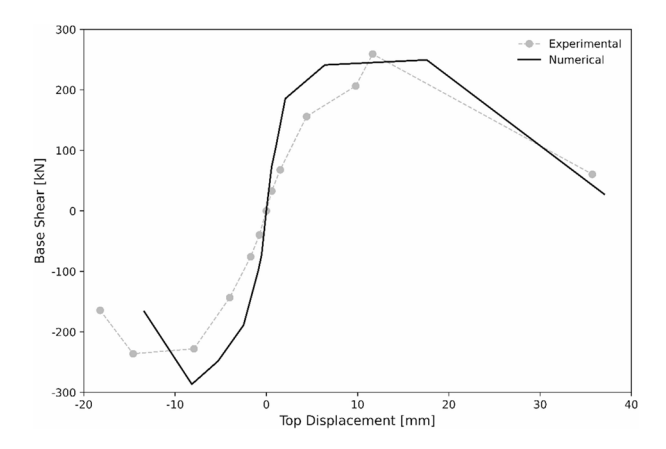


Fig. 11 Numerical and experimental displacement time histories for a Test 3, b Test 5





onward. The numerical and experimental multi-linear envelopes are shown in Fig. 12. While the numerical model developed a stiffer response in the first cycles, a better agreement was obtained in later stages. Indeed, the numerical model achieved a near-collapse condition during Test 5 (PGA=0.63g). Maximum capacity was estimated in about -4% error, and residual capacity (both in the positive and negative directions) is appreciably close to its experimental counterpart. Experimental damage progression, as described in (Kouris et al. 2019) was also captured: at the end of Test 3 (PGA=0.32g), cracking phenomena mainly involved the spandrels according to experimental observations. In the subsequent tests, the numerical model also experienced major cracking within the main gable façade, in good



agreement with experimental evidence. Ultimately, in Test 5 (PGA=0.63g), the OOP and IP damage observed experimentally could be reproduced with good agreement by plotting cracked springs (see Fig. 13), that is, springs which failed in tension and/or shear but may still withstand compressive loads.

It is worth noting that the numerical crack pattern was able to capture experimental damage of both the East and West façades, mainly concentrated at spandrel ends and, at first storey, within the spandrels themselves (see spandrels W-7 and W-8). Rocking failures of West façade piers were also captured (see piers W-2 and W-6). With regards to OOP damage, numerical crack pattern highlights the occurrence of a gable mechanism in the North façade, though the numerical model did not capture the sub-vertical crack passing through the gable. The sub-vertical crack in spandrel N-5 was also captured, particularly at spandrel end rather than close to the centroid. The crack at the base of Pier N-1 was also hinted at. With regards to the South facade, the model was able to capture its gable sub-vertical crack; however, base gable cracks were not captured. This may be due to early sliding failure between the ridge beam and the South gable, which may have reduced coupling between the two gables and pre-empted full development of an overturning mechanism for the South façade. Other differences may be explained by the variability of material properties and the effects of bond pattern irregularities, which could not be captured through a deterministic approach (see, e.g., (Pulatsu et al. 2023a). Nevertheless, it should be noted that these discrepancies do not seem to have undermined the numerical model's performance in terms of PRDs, displacement trend, and global shear capacity.

It is also noted that this benchmark was considered also in other studies based on different modelling strategies. However, no direct comparison can be drawn with regards to (Costa et al. 2015; Kouris et al. 2022), as both studies had a different focus and did not delve deep into fracture mechanics nor cumulative damage simulation. Some considerations can be drawn, however, with regards to (Tomić et al. 2021), who made use of EFM to simulate the specimen's damage progression and failure mechanism. With regards to displacement

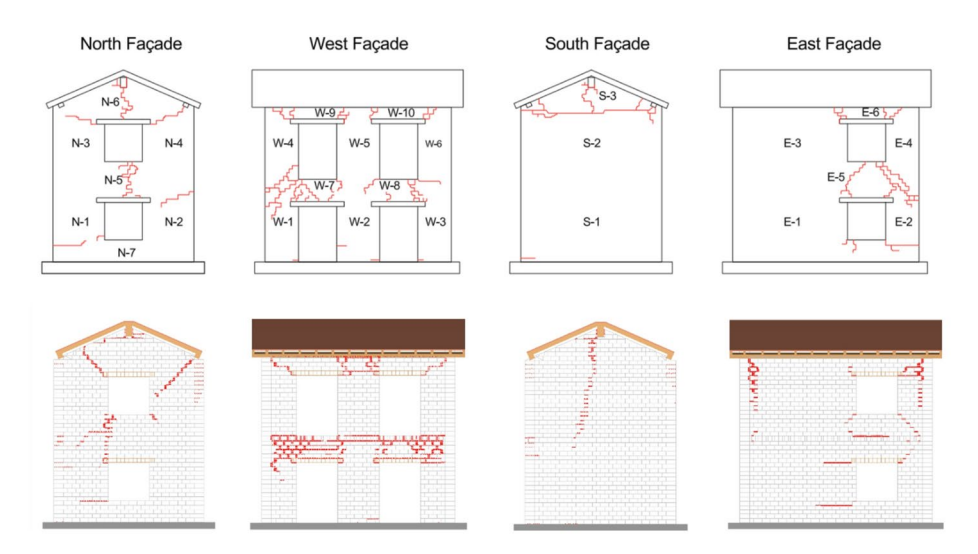


Fig. 13 Comparison between the experimental crack pattern sketch, adapted from (Guerrini et al. 2021), and the numerical cracked springs distribution. Only crack widths larger than 2.5 mm are shown)



behaviour, a comparison is only possible in terms of PRDs, which were captured with comparable accuracy within both studies. The EFM model also captured the specimen's collapse mechanism, but detailed damage simulation within macro-elements themselves could not be achieved, as it could instead be in a discontinuum framework such as the AEM approach used in the present paper. Indeed, a good agreement was also obtained by the AEM subassemblage model developed by (Morandini 2022), both in terms of failure mechanism and displacement time history. Interestingly, the sub-assemblage model was also able to capture the overturning of the South gable, which was not captured here due to reduced coupling between the masonry and the ridge beam. Nonetheless, it should be noted that the sub-assemblage model was subjected to a single ground motion record, with PGA=0.40g and damage accumulated by the physical specimen during previous test runs being deterministically incorporated within the AEM model. This may hold significant implications with regards to the predictive capacity of the model. In the present study, on the other hand, damage progression and accumulation were explicitly accounted for, starting from an undamaged condition, showcasing the suitability of the AEM in satisfactorily reproducing the experimental behaviour in terms of displacements, damage accumulation and failure modes.

6 Sensitivity of seismic performance and damage to masonry quality

6.1 Assumptions

The validated model was further investigated to assess variations in seismic performance and collapse mechanisms of the reference building, considered representative of Italian vernacular architecture, as a function of masonry quality. Therefore, such a sensitivity analysis allowed testing the AEM's capability in predicting complex failure mechanisms of URM buildings subjected to strong ground motion, accounting for the role of masonry quality and associated properties. Furthermore, this also offered the opportunity to test the suitability of novel damage measures, based on explicit cracking simulations, in seismic performance assessment of URM buildings. To this aim, the reference values of masonry mechanical parameters calibrated over the experimental results in (Magenes et al. 2010c) were subjected to $\pm 10\%$ variations till $\pm 50\%$ as outlined in Table 4. All masonry properties were amplified or de-amplified at once, to deterministically account for masonry quality variations due to the scatter in constituents and workmanship. This resulted into a range of material properties which, in agreement with the (Circolare n°7, 21.01.2019), can be seen as representative of various regularly and irregularly coursed stone masonry typologies found in existing Italian buildings.

Ground motion recorded during August 24th, 2016, Amatrice earthquake was taken as a reference strong shaking for collapse analysis. Based on specimen geometry and the input ground motion characteristics, simulations are expected to yield complex OOP fail-

Table 4 Mechanical properties considered within the parametric analysis

Value	Е	G	f _c	f _t
	[MPa]	[MPa]	[MPa]	[MPa]
Lower bound	750	250	1.64	0.07
Reference	1500	500	3.28	0.14
Higher bound	2250	750	4.92	0.21



ure mechanisms, to be then compared with actual field data discussed in (Fiorentino et al. 2018; D'Ayala et al. 2019). Acceleration time histories recorded by AMT station (Amatrice, 42.632460° latitude, 13.286176° longitude, 950 m elevation, type B soil according to EC8) was selected due to station proximity (approximately 3 km) to the rupture fault. The original record duration is 27.89 s, with a sampling interval $\Delta t = 0.005$ s. The two horizontal acceleration components were characterised by PGA values equal to 0.87g and 0.38g, respectively. The two time-history records (Fig. 14) are referred to as 'strongest' and 'weakest', respectively, with reference to the absolute peak values.

Both records were applied simultaneously and two analyses per numerical specimen were run, rotating the ground motion components by 90° while keeping the same orientation. The aim was two-fold: (i) to generate stronger OOP loads on either the gables or the longitudinal walls, depending on the direction of the strongest acceleration record; and (ii) to observe a higher number of damage and/or collapse configurations. Therefore, the variability in ground motion direction and mechanical properties led to a total of 22 analyses and multiple damage configurations. Analyses were run using a 16 GB RAM, AMD Ryzen 7 4700U (2 GHz) processor-equipped machine and took approximately 1 h each.

6.2 Proposal for novel crack width-based damage measures

The appealing feature of AEM to explicitly account for damage spread and fracture phenomena motivated the formulation and testing of crack width-based damage measures. According to the adopted constitutive laws, failure criteria and post-failure mechanical behaviour, spring strains produce finite displacements, which can be easily extracted from the AEM model in Extreme Loading for Structures software (ASI 2021). Thus, performance assessment in terms of damage spread and severity becomes possible, provided that meaningful damage measures are identified. In this study, damage propagation in the masonry is accounted for through a Crack Propagation Ratio (CPR) defined as per Eq. 5:

$$CPR = \frac{n}{N} \tag{5}$$

where n is the sum of URM springs in either cracked (springs incurring into tensile failure, with residual compressive and frictional strength) or separated (strain norm exceeding separation strain ε_s) state, and N is the total number of URM springs. CPR can be consid-

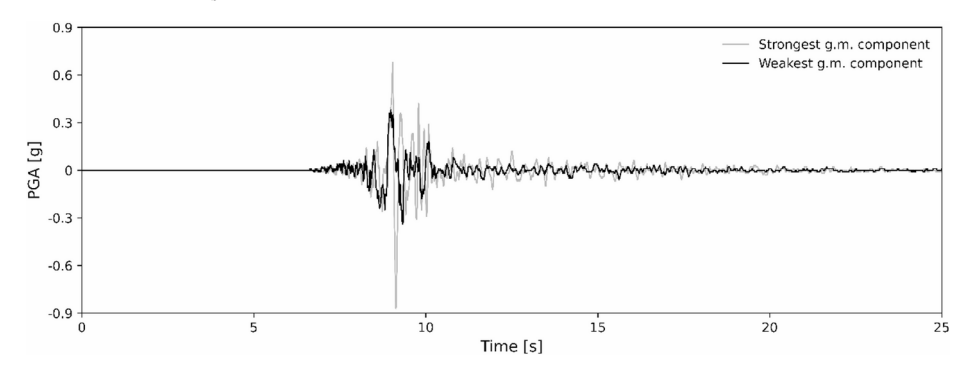


Fig. 14 Acceleration time histories input for August 24th, 2016, Amatrice earthquake (AMT station)



ered as a local damage index because it ranges between 0 and 100% and, in the hypothesis of regularly spaced rigid elements, is directly proportional to cracked masonry volume. The definition of DMs able to quantify cracking severity, on the other hand, may not be as straightforward to define, as they are conditional on the adopted grading criterion. A widely adopted framework in seismic damage assessments is that provided by the European Macro-Seismic Scale (EMS-98, Grünthal et al. 1998), which categorises damage into five damage grades (from Grade 1, negligible to slight damage, up to Grade 5, complete or near-complete collapse). However, a notable shortcoming of EMS-98 lies in its reliance on qualitative descriptions of damage. In this respect, it should be noted that, while crack widths may be taken as quantitative indicators of structural damage, their relationship with the residual load-bearing capacity or safety of structures is not yet fully explored and understood. Further research into the topic is indeed required before crack width-based damage grading criteria may be introduced. Indeed, researchers have only recently begun tackling the issue of damage grading of URM structures within discontinuum frameworks (Korswagen et al. 2019; Sarhosis et al. 2021). For instance, in (Korswagen et al. 2019), a dimensionless damage parameter ψ was introduced and normalised based on crack number and width. A notable shortcoming lies in this parameter having been calibrated only for crack widths lower than 5 mm, that is, for slight damage conditions. It should also be considered that accounting for crack number may require the implementation of user-defined subroutines and lead to misleading results due to crack coalescence occurrence (which would yield a lower crack number, and thus lower damage grading). In (Sarhosis et al. 2021), the proposed dimensionless damage parameters account for both slip and tensile failures, as well as achievement of ultimate drift, thus being mainly aimed at IP damage grading. Furthermore, damage parameters are normalised based on crack lengths, which retrieval may again require user-defined sub-routines. To overcome the issues above, a simpler approach is proposed in this study and is based on simple mechanical observations on URM behaviour, coupled with a repairability-based approach. A negligible to slight damage condition was associated with principal tensile strains between cracking strain ε_{cr} defined as the ratio between tensile strength and Young's Modulus – and an ultimate tensile strain $\varepsilon_{t,u}$ associated with complete bond degradation. Ultimate tensile strain is defined according to Eq. 6 as a function of tensile strength f_t , tensile fracture energy G^f and crack bandwidth h, resulting into crack widths between 0.1 mm and 0.2 mm, that is, the minimum crack widths (so-called "hairline cracks") observed by naked eye (Burland and Wroth 1974; Reagan et al. 2018).

$$\varepsilon_{\rm t,u} = \frac{2G^{\rm f}}{hf_{\rm t}} \tag{6}$$

According to (EC6 2005), crack widths lower than 10 mm may be sealed through mortar repointing or cement grouting; thus, this was taken as a further crack width threshold to denote a slight damage condition. Wider cracks may require more substantial intervention, such as stitching or resetting units within new mortar. Excessive unit sliding over cracked joints may then compromise stability, as displacements larger than 1/6 of unit length L or 1/6 of unit thickness t may result into a loss of alignment, occurrence of additional bending onto already cracked joints, localised unit crushing due to excessive axial stresses, and possible buckling or collapse under OOP loads. Accordingly, the transition from moderate to severe damage condition is here associated with a 33 mm crack width (1/6 of unit length),



which is associated in turn with the numerically calibrated separation strain value ε_s = 0.15. In this study, a choice was made to consider four different damage levels – negligible, slight, moderate and severe – associated with the approximate principal tensile strain values and crack width thresholds outlined in Table 5.

By considering the ratio between the number *m* of springs in any of these given conditions, and the total number of failed springs *n*, four novel Damage Ratios can be introduced as follows: Negligible Damage Ratio (NDR); Light Damage Ratio (LDR); Moderate Damage Ratio (MDR); Severe Damage Ratio (RDR). This makes damage parameter normalisation more straightforward. Furthermore, both slight and severe damage is accounted for, regardless of whether this is due to IP or OOP failures. Thus, although overall damaged volume may be estimated through CPR (Eq. 5), severity of such damage can be attributed to four separate damage ratios and accounted for by means of damage indexes complementary to each other. When coupled with repair or reconstruction unitary costs, DMs thus conceived may be used to assess economic losses due to extension and severity of damage. Furthermore, while such damage measures are here adopted to grade damage spread and severity at the end of the analysis, these could also be used to grade cumulative damage within methodologies such as Incremental Dynamic Analysis (IDA) or within fragility assessment frameworks.

6.3 Challenges and opportunities in crack width-based damage grading

As previously noted, residual crack widths are an easily monitorable and measurable damage indicator, both via simple tools such as crack gauges, as well as more advanced, visual databased methods; see (Korswagen et al. 2019, 2020; Asjodi and Dolatshahi 2023). Indeed, damage grading approaches based on residual crack width are commonly used in structural engineering, particularly after events like earthquakes, to assess structural condition. For instance, FEMA 306 guidelines (1998) provide different residual crack width thresholds, distinguishing between shear and flexural failures at macro-element scale, with reference to four different damage conditions (insignificant, moderate, severe and extreme). A similar approach is pursued in the AeDES guidelines (Baggio et al. 2007), which notes different crack width threshold depending on damage level and the observed failure mechanism. However, both referenced guidelines do not provide thresholds for higher levels of damage, relying instead on a phenomenological description (e.g. attainment of crushing, failure mechanism activation, and so on). The relationship between failure mechanism, crack width severity and distribution, and macro-element-scale residual stiffness and strength is in fact, as previously noted, yet to be thoroughly explored. To this aim, several works have been developed with an aim to establish correlations between residual crack width, maximum and/or residual macro-element drift and damage state attainment; see (Magenes et al. 2010b; Korswagen et al. 2019; Rezaie et al. 2021; Asjodi and Dolatshahi 2023). Future developments in these regards may significantly contribute to the applicability and reliabil-

Table 5 Principal tensile strain and approximate crack width ranges adopted within the proposed damage grading procedure

Damage description	Strain range [%]	Approximate crack width [mm]
Negligible to slight	$\varepsilon_{cr} \le \varepsilon < \varepsilon_{t,u} = 0.09$	$0 \le w < 0.20$
Light	$0.09 \le \varepsilon < 4.60$	$0.20 \le w < 10.00$
Moderate	4.60≤ε<15	$10.00 \le w < 33.00$
Severe	$\varepsilon \ge \varepsilon_{\rm s} = 15$	<i>w</i> ≥33.00



ity of crack-width-based damage grading, and may also be pursued via advanced numerical modelling, as shown by the developments here discussed.

According to the previously referenced guidelines (FEMA 306, 1998; Baggio et al. 2007), in the presence of a complex crack pattern, damage severity classification is governed by the widest crack. It is noted, however, that maximum crack width may be significantly larger than the average width of a series of parallel cracks, and may thus be, depending on crack pattern features, better suited to describe localized damage, rather than element-scale or building-scale damage severity. A further shortcoming resides in crack widths being often only measurable on the outer faces of a masonry element, and, hence, not being able to fully describe the internal damage condition of double leaf or rubble core masonry walls. Similar issues also apply to plastered elements; interesting developments have been discussed, in these regards, in (Calderini et al. 2015), which aimed at developing correlations between structural damage and damage on artistic assets. A similar experimental investigation has also been carried out in (Rezaie et al. 2021).

Despite the limitations discussed above, residual crack widths remain, however, a practical and widely applicable proxy for damage assessment, offering a balance between simplicity, accessibility, and meaningful correlation with structural performance, particularly when integrated with an understanding of crack patterns, failure mechanisms, element-scale deformation parameters and complementary diagnostic methods.

6.4 Analysis results

The parametric analysis yielded multiple post-earthquake damage configurations, ranging from complete collapse to moderate damage conditions and some degree of residual loadbearing capacity being retained, depending on the activated failure modes. An analysis of the observed damaged configurations at the end of time-histories was performed. Complex failure mechanisms, resulting from a combination of elementary failure mechanisms at element or wall scale, were observed. The failure mechanisms at element or wall scale are as follows (Fig. 15): (a) IP response, associated with spandrel flexural failure; (b) second storey rigid body overturning; (c) second storey spandrel overturning; (d) corner overturning, possibly involving adjacent spandrels: (e) gable failure due to overturning mechanism or lintel stability loss. Such collapse mechanisms are in good agreement with those recorded in (Fiorentino et al. 2018; D'Ayala et al. 2019). Transition from IP- to OOP-dominated behaviour was observed under -10% variation in reference mechanical properties. The occurrence of OOP failures in lower quality masonry specimens is in good agreement with field data (Fiorentino et al. 2018; D'Ayala et al. 2019), according to which poor-quality mortar joints, poor connection between walls and floors, poor cross-sectional connections and poor wall-to-wall connections were the main causes of OOP mechanism activation. Nonetheless, it should be noted that the latter two aspects could not be here captured due to modelling assumptions; indeed, the numerical modelling of rubble masonry and multi-leaf masonry with rubble cores is an aspect which calls for further investigation, especially within discontinuum modelling techniques (Adhikari and D'Ayala 2020; Malomo and Pulatsu 2024).

It should be noted, again, that these elementary collapse mechanisms may combine with each other, leading to quite complex failure patterns. Figure 16 details one of such instances, that, is, the simultaneous NE corner and W façade overturning at the second storey, which was observed to occur for the lowest quality model (reference mechanical



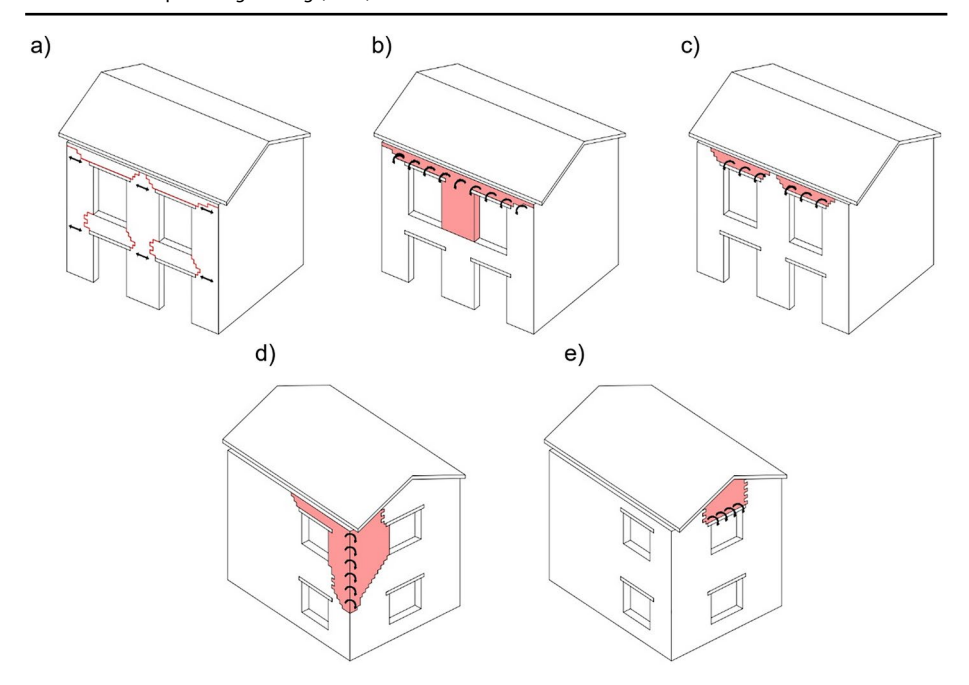


Fig. 15 Elementary collapse mechanisms observed at the end of nonlinear time histories

properties decreased by 50%) in both loading scenarios (that is, regardless of whether higher PGA values acted transversal or parallel to the façades). The combined effects of the pitched roof thrust and transversal ground motion activated an OOP response of both the NE corner macro-element (Fig. 16a) and the West façade pier and spandrel elements at the upper storey (Fig. 16b). This caused, in turn, the loss of support for the roof itself (Fig. 16c), leading to debris impacts with the timber floor and floor failure. The final configuration can be observed in Fig. 16d. Post-processing of AEM results, based on filtering of separated elements according to their coordinates and volume, allowed the prediction of both inward (4.5 m³) and outward (5 m³) debris projection, resulting in approximately 33% loss of total structural volume.

The activation of second-storey wall overturning mechanisms (Fig. 15b) was found to yield severe consequences, due to either the loss of support to roof structures or URM debris projection over timber floors. Indeed, if spreader beams along longitudinal walls retain simple end support conditions, roof collapse may be prevented. Inward projection of URM debris may still cause severe damage to the floors, causing their collapse and likely causing many fatalities. It is noted that also gable failures (Fig. 15e) may trigger progressive collapse scenarios, due to loss of support to roof elements. By contrast, whenever OOP mechanisms did not activate and/or roof connections did not fail, a more IP-dominated response emerged through spandrel flexural failures. It seems thus apparent that lack of structural redundancy within roof members and OOP failure activation may play a significant role in collapse occurrence. Correlation between masonry quality, crack propagation and crack severity can be qualitatively observed in Fig. 17, where damage distribution at the end of the



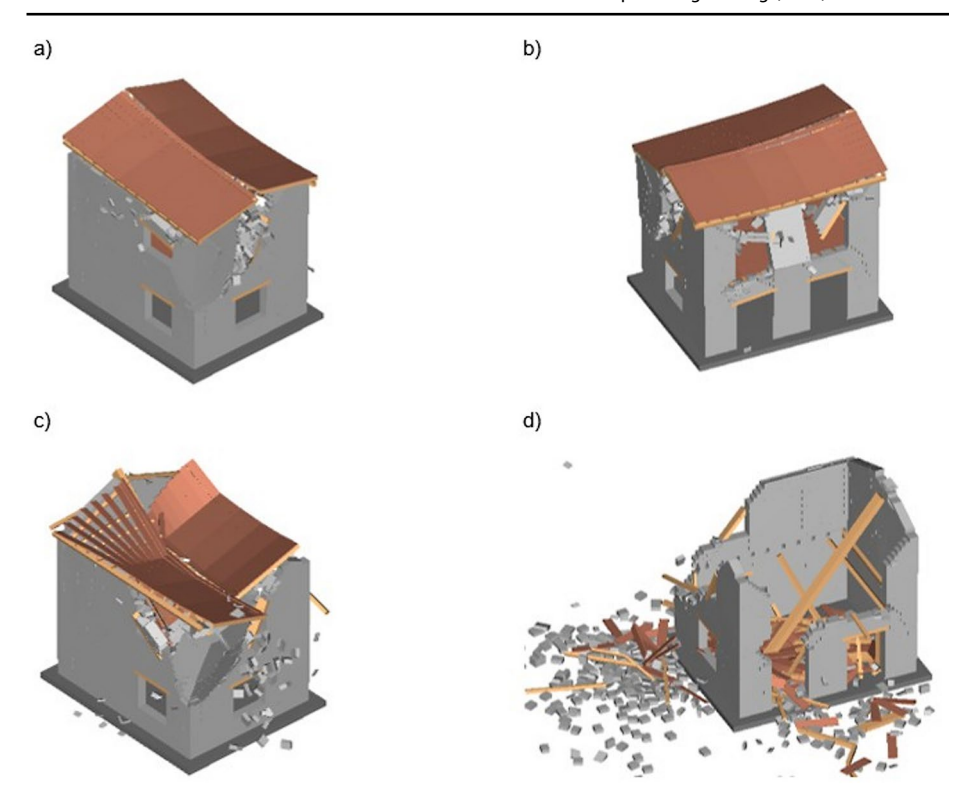


Fig. 16 Progressive collapse sequence observed for lower masonry quality models

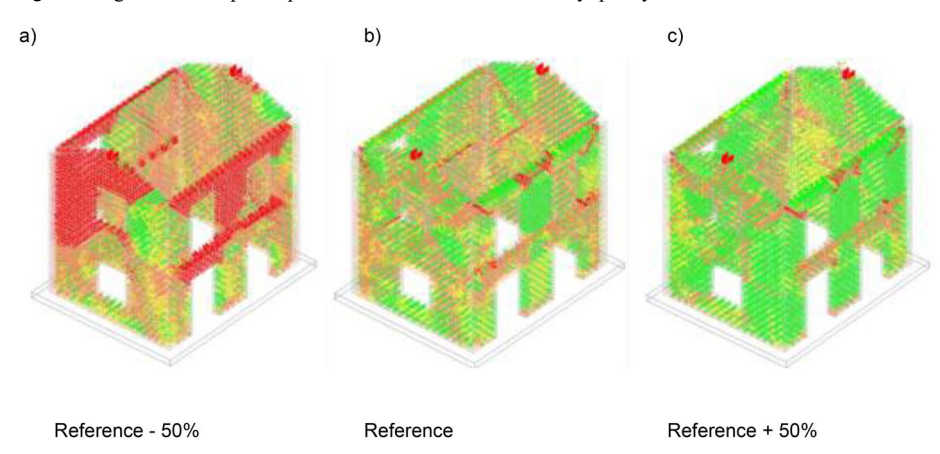


Fig. 17 Distribution of undamaged (green), negligibly damaged (yellow), lightly damaged (orange), moderately and severely damaged (red) URM over specimen undeformed configuration

analysis performed under $PGA_x = 0.87g$ and $PGA_y = 0.38g$ is plotted over the undeformed configuration for models with -50% variation (Fig. 17a), reference values (Fig. 17b) and +50% variation (Fig. 17c) of masonry quality, respectively. Both West wall and NE corner overturning mechanism can be observed in Fig. 17a, whereas effects of masonry quality



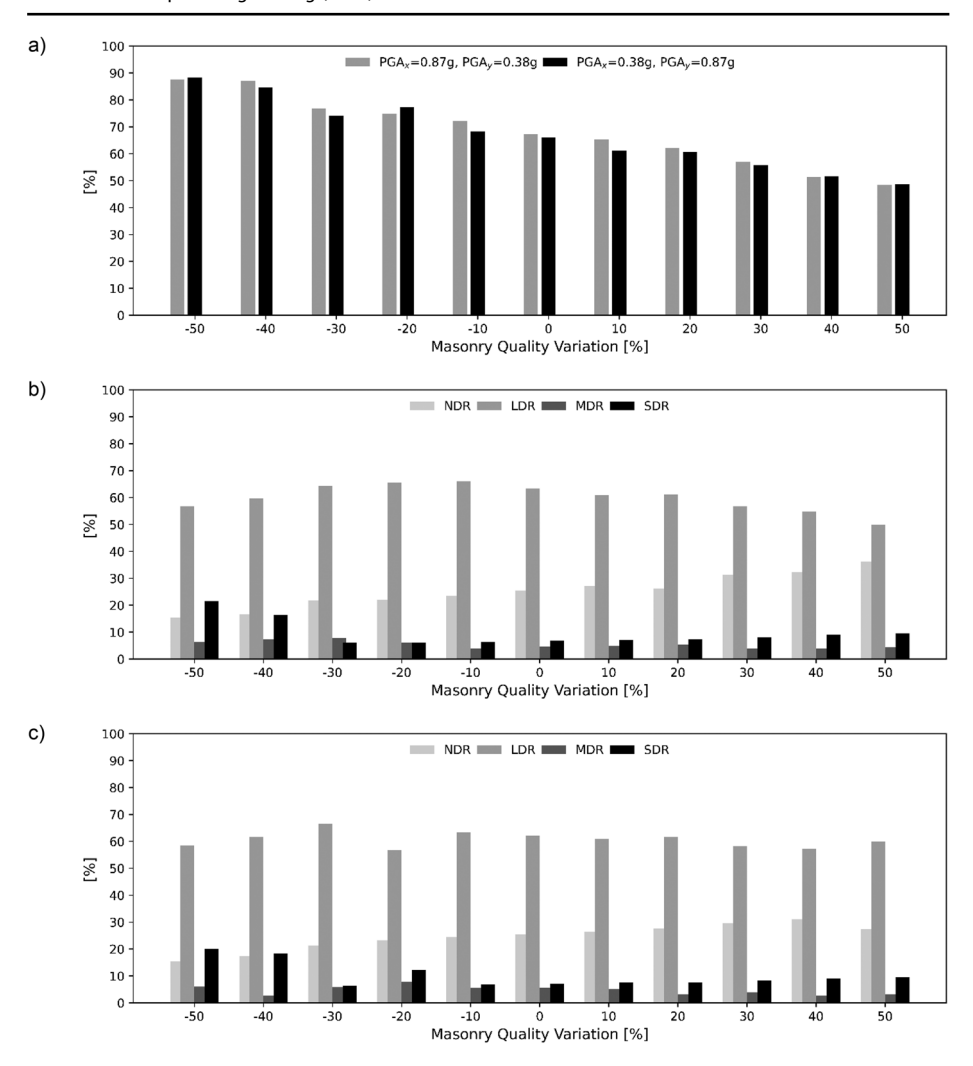


Fig. 18 Variability of the proposed novel damage parameters as a function of masonry quality variations: a CPR variability in both loading scenarios; damage severity ratios for **b** strongest ground motion intensity along X-direction $(PGA_x = 0.87g, PGA_y = 0.38g)$ and **c** strongest ground motion intensity along Y-direction $(PGA_x = 0.38g, PGA_y = 0.87g)$

increase on the extent of undamaged masonry (green) and damage localisation within spandrels can also be detected in Fig. 17b and c.

Remarkable differences in structural performance are outlined by the previously introduced damage measures, CPR (Crack Propagation Ratio), NDR (Negligible Damage Ratio), LDR (Light Damage Ratio), MDR (Moderate Damage Ratio) and SDR (Severe Damage Ratio). Figure 18a details CPR variability as a result of negative (down to -50%) and positive (up to +50%) variations with respects to reference mechanical properties. The model with reference mechanical properties achieved CPR values approximately equal to 67% in both loading conditions. The CPR varies between 88% (50% decrease in masonry quality) and 48% (50% increase in masonry quality). A clear trend emerges between increasing



masonry quality and a reduction in damaged masonry volume, regardless of whether the stronger ground motion is oriented parallel (PGA_x = 0.87 g, PGA_y = 0.38g) or perpendicular (PGA_x = 0.38g, PGA_y = 0.87g) to the longitudinal walls in the X-direction. Figure 18b and c highlight that the higher the masonry quality increase, the higher the extent of negligibly damaged masonry volume, that is, the share of hairline cracks (w<0.2 mm); positive variations in mechanical properties can in fact be observed in association with a rise in NDRs. By contrast, both LDR and MDR do not seem significantly influenced by masonry quality; however, when coupled with a global reduction in CPR as a function of masonry quality, these hint at a reduction of both slightly and moderately damaged masonry volume. Ultimately, SDR can be observed to sharply reduce under -10% variation in masonry quality, which was also observed as a threshold between OOP-dominated and IP-dominated response. Transition values of masonry properties were identified as follows: E=1,350 MPa, G=350 MPa, f_c =2.95 MPa, f_t =0.12 MPa. It should be noted that these values are conditional on specimen geometry, boundary conditions and input ground motion, so care should be paid before their possible use as a general reference.

Counter-intuitively, SDR seems to gradually increase as a function of masonry quality, so its nature as a relative indicator should be taken into account to understand this phenomenon. This is consistent with a transition from OOP-dominated to IP-dominated mechanisms and such IP-dominated behaviour is characterised by damage localisation at spandrel ends, in the form of flexural cracks. A susceptibility to experience larger crack displacements in those areas was also observed, both in the referenced experimental campaign (Magenes et al. 2010c), the numerical simulation of the experimental tests, and the sensitivity analysis discussed in this section. By increasing masonry quality, the number and extent of severely opened cracks progressively tends to settle onto a fixed value, which represents the head and bed joints involved in the spandrel flexural cracks. The stabilisation of the number of severely opened cracks (denoted by m), coupled with a reduction in the number of failed springs (denoted by n), leads to an increase in SDR.

Based on the above discussion, AEM simulations were able to highlight potential failure mechanisms of non-symmetrical URM buildings with flexible diaphragms under strong biaxial ground motion. The role of masonry quality into the occurrence of OOP failure mechanisms was highlighted, as well as the impact of low structural redundancy associated with floor and roof systems on the occurrence of progressive collapses. Given the same geometry and boundary conditions, an increase in values of mechanical properties played a key role in delaying the onset of overturning failure mechanisms to higher levels of ground motion intensity, allowing the numerical specimens to develop an IP-dominated behaviour by concentrating damage within spandrels. This was also captured through the crack width-based DMs proposed in this study, which were able to track progressive reduction in both damage spread and severity as a function of increasing masonry quality.

7 Conclusions

URM buildings subjected to severe loading conditions develop a quasi-brittle response, which is often characterised by OOP mechanisms and complex failure sequences. This study aimed at investigating the suitability of Applied Element Method (AEM) to realistically simulate the expected near-collapse and beyond-collapse behaviour of URM assemblies



and buildings. A micro-modelling approach was adopted, lumping material nonlinearities in unit-to-unit contact springs. The experimentally observed shaking-table response of URM specimens with different masonry type, size and geometry was then simulated. The validated models were then used into a sensitivity analysis to assess the variability in the structural response of non-symmetrical buildings, subjected to strong biaxial ground motion, as a function of deterministic variations in masonry quality. The following findings can be drawn:

- Good numerical-experimental agreement was observed at both wall assembly and building scales, in terms of displacement time histories, collapse loads, damage progression, and failure mechanisms.
- Compared with other continuum-based and discontinuum-based modelling strategies, the AEM was also able to accurately predict the overall volume involved in the collapse mechanism, as well as debris trajectories. This holds significant implications with regards to the use of the AEM as a predictive tool, to support building and urban scale resilience assessments.
- URM axial and tangential stiffness parameters had to be significantly decreased to capture experimental displacements and/or frequencies; this was also observed in other AEM numerical studies and may hint at an over-stiffening effect. It should indeed be noted that, within discontinuum methods, the number of contact points may significantly affect global stiffness, as pointed out in (Malomo and Pulatsu 2024). To work around the issue while keeping in check contact point number, and hence computational burden, calibration procedures such as those described in (Malomo et al. 2018) may be used, adjusting elastic parameters to match theoretical or experimental system stiffness.
- Acceleration capacity and failure mechanisms were captured through experimental strength values, which is not always the case in AEM-based numerical studies. This may be explained by the choice of fracture energy-based softening laws over the brittle failure models often adopted in the AEM. Such a conclusion is consistent with outcomes of DEM studies, such as (Pulatsu et al. 2019; Pulatsu 2023), while dealing with the simulation of quasi-brittle mechanics via advanced elasto-softening constitutive laws in tension, compression and shear. Thus, the use of fracture energy-based softening laws within an AEM framework should be encouraged to improve accuracy and to reduce calibration efforts.
- The sensitivity analysis enabled both the identification of recurrent elementary mechanisms and the simulation of their complex interactions. A transition from an OOP-dominated response to a more IP-dominated response was observed under −10% decrease in reference masonry quality. Progressive collapse instances were observed under lower masonry quality models, because of OOP failure occurrence and lack of redundancy of floor and roof structures.
- Novel damage measures were introduced to explicitly account for cracking propagation and severity. As expected, an inverse proportionality was found between extent of cracked URM volume and masonry quality. To that aim, a Crack Propagation Ratio was proposed based on the occurrence of tensile and/or shear failures. Damage severity was then quantified through residual crack widths and a repairability criterion based on code provisions and simple mechanical criteria.



Future developments of this study might include the use of the proposed damage measures to predict direct economic losses in the form of repair costs. Potential limitations of this approach may, however, lie in the lack of a more nuanced damage grading – able to more accurately consider, for instance, cracking effects over element stability and load-bearing capacity – as well as in the inability to account for failure propagation within floor and roof systems. Further studies may thus focus on such aspects, as well as the development of a damage grading criterion that might be consistent with those typically used in seismic damage assessment (e.g., EMS-98 scale)."

Acknowledgements This study was developed within the framework of FAIL-SAFE project ("near-real-time perFormance Assessment of exIsting buiLdings Subjected to initAl Failure through multi-scalE simulation and structural health monitoring", Grant No. P2022X7N2S_002, CUP N.E53D23003350006), which was funded by European Union through Next-GenerationEU programme - National Recovery and Resilience Plan (PNRR) - Mission 4, Component 2, Investment 1.1, PRIN 2022 programme of the Italian Ministry of University and Research (D.D. 02/02/2022, n.104; PI: Fulvio Parisi). The authors would, furthermore, like to acknowledge the funding and support provided by University of Naples Federico II by means of its International Mobility scheme. The authors would like to thank Prof. Paulo Lourenço and Dr. Nuno Mendes from University of Minho, as well as Prof. Andrea Penna and Dr. Ilaria Senaldi from University of Pavia, for kindly sharing the experimental data here taken as benchmark. Finally, the first author would like to acknowledge the support by Applied Science International, LLC, as well as its Senior Structural Consultant, Ayman Elfouly, for the technical guidance on the use of the AEM-based "Extreme Loading for Structures" software employed within this study.

Author contributions Conceptualization: Fulvio Parisi and Dina F. D'Ayala; Methodology: Ciro Canditone, Fulvio Parisi and Dina F. D'Ayala; Formal analysis and investigation: Ciro Canditone, Fulvio Parisi, Dina F. D'Ayala and Arianna Guardiola-Villora; Writing - original draft preparation: Ciro Canditone; Writing - review and editing: Fulvio Parisi, Dina F. D'Ayala and Arianna Guardiola-Villora; Funding acquisition: Fulvio Parisi; Resources: Fulvio Parisi; Supervision: Fulvio Parisi and Dina F. D'Ayala.

Funding Open access funding provided by Università degli Studi di Napoli Federico II within the CRUI-CARE Agreement. Open access funding provided by Università degli Studi di Napoli Federico II within the CRUI-CARE Agreement. This study was funded by European Union through Next-GenerationEU programme - National Recovery and Resilience Plan (PNRR) - Mission 4, Component 2, Investment 1.1, PRIN 2022 programme of the Italian Ministry of University and Research (D.D. 02/02/2022, n.104; PI: Fulvio Parisi). Open access funding was provided by University of Naples Federico II within the CRUI-CARE Agreement.

Data availability Data will be made available upon request.

Declarations

Conflict of interest The authors have no conflict of interest to declare.

Open Access This article is licensed under a Creative Commons Attribution 4.0 International License, which permits use, sharing, adaptation, distribution and reproduction in any medium or format, as long as you give appropriate credit to the original author(s) and the source, provide a link to the Creative Commons licence, and indicate if changes were made. The images or other third party material in this article are included in the article's Creative Commons licence, unless indicated otherwise in a credit line to the material. If material is not included in the article's Creative Commons licence and your intended use is not permitted by statutory regulation or exceeds the permitted use, you will need to obtain permission directly from the copyright holder. To view a copy of this licence, visit http://creativecommons.org/licenses/by/4.0/.



References

- Adhikari R, D'Ayala D (2020) Nepal earthquake: seismic performance and post-earthquake reconstruction of stone in mud mortar masonry buildings. Bull Earthq Eng 18(8):3863–3896
- Adhikari R, Parammal-Vatteri A, D'Ayala D (2023) Seismic performance assessment of Low-Rise unreinforced and confined brick masonry school buildings using the applied element method. Buildings 13(1):159
- Al-Shawa O, Sorrentino L, Liberatore D (2017) Simulation of shake table tests on Out-of-Plane masonry buildings. Part (II): combined Finite-Discrete elements. Int J Architectural Herit 11(1):79–93
- ASI (2021) Extreme loading for structures v8. Applied Science International, LLC, Durham, USA
- Asjodi AH, Dolatshahi KM (2023) Extended fragility surfaces for unreinforced masonry walls using visionderived damage parameters. Eng Struct 278:115467
- Augenti N, Parisi F (2010) Learning from construction failures due to the 2009 l'aquila, italy, earthquake. J Perform Constr Facil 24(6):536–555
- Augenti N, Parisi F (2011) Constitutive modelling of tuff masonry in direct shear. Constr Build Mater 25(4):1612-1620
- Baggio C, Bernardini A, Colozza R, Corazza L, Della Bella M, Di Pasquale G, Dolce M, Goretti A, Martinelli A, Orsini G (2007) Field manual for Post-Earthquake damage and safety assessment and Short-Term countermeasures (AeDES). European Commission Joint Research Centre Institute for the Protection and Security of the Citizen
- Bui T, Limam A, Sarhosis V, Hijaj M (2017) Discrete element modelling of the in-plane and out-of-plane behaviour of dry-joint masonry wall constructions. Eng Struct 136:277–294
- Burland J, Wroth C (1974) Settlement of buildings and associated damage. Cambridge, PentechPress, Proceeding of Conference on Settlement of Structures
- Calderini C, Degli Abbati S, Coti P, Kržan M, Bosiljkov V (2015) In-plane shear tests on masonry panels with plaster: correlation of structural damage and damage on artistic assets. Bull Earthq Eng 13:237–256
- Calò M, Malomo D, Gabbianelli G, Pinho R (2021) Shake table response simulation of a URM Building specimen using discrete micro models with varying degrees of detail. Bull Earthq Eng 19:5953–5976
- Candeias PX, Campos Costa A, Mendes N, Costa AA, Lourenço PB (2017) Experimental assessment of the Out-of-Plane performance of masonry buildings. Int J Architectural Herit 11(1):31–58
- Canditone C, Parisi F (2024) Numerical Simulation of Soft Stone Masonry Under Simple Compression Using the Applied Element Method. In: Proceedings of WCEE 2024–18th World Conference on Earthquake Engineering, Milan, Italy
- Canditone C, Diana L, Formisano A, Rodrigues H, Vicente R (2023) Failure mechanisms and behaviour of Adobe masonry buildings: A case study. Eng Fail Anal 150:107343
- Chácara C, Mendes N, Lourenço PB (2017) Simulation of shake table tests on Out-of-Plane masonry buildings. Part (IV): macro and Micro FEM approaches. Int J Architectural Herit 11(1):103–116
- Chácara C, Cannizzaro F, Pantò B, Caliò I, Lourenço PB (2018) Assessment of the dynamic response of unreinforced masonry structures using a macroelement modelling approach. Earthquake Eng Struct Dynam 47(12):2426–2446
- Circolare, n°7 21.01.2019 (2019) istruzioni per l'applicazione dell'«aggiornamento Delle Norme tecniche per Le costruzioni». Rome, Italy: Ministero delle Infrastrutture
- Costa A, Penna A, Arêde A, Costa A (2015) Simulation of masonry out-of-plane failure modes by multibody dynamics. Earthquake Eng Struct Dynam 44(14):2529–2549
- Cundall P (1971) A computer model for simulating progressive large-scale movements in blocky rock systems. Nancy, France
- Cundall P (1988) Formulation of a three-dimensional distinct element model Part I: A scheme to detect and represent contacts in a system composed of many polyhedral blocks. Int J Rock Mech Min Sci 25(1):107–116
- D.M. 17.01.2018 (2018) Norme tecniche per Le costruzioni. Rome, Italy: Ministero delle Infrastrutture e dei Trasporti
- D'Ayala D (2005) Force and displacement based vulnerability assessment for traditional buildings. Bull Earthq Eng 3:235–265
- D'Ayala D (2013) Assessing the seismic vulnerability of masonry Building. In: Tesfamariam S, Goda K (eds) Handbook of seismic risk analysis and management of civil infrastructure systems. Woodhead Publishing Series in Civil and Structural Engineering, pp 334–365
- D'Ayala D, Speranza E (2003) Definition of collapse mechanisms and seismic vulnerability of historic masonry buildings. Earthq Spectra 19(3):479–509



- D'Ayala DF, Walker J, Mildon Z, Lombardi D, Galasso C, Putrino V, De Luca F, Del Gobbo G, Lloyd T, Morgan EC, Totaro A, Alexander D, Tagliacozzo S (2019) The Mw 6.2 Amatrice, Italy Earthquake of 24th August 2016. Earthquake Engineering Field Investigation Team (EEFIT)
- D'Ayala D, Paganoni S (2011) Assessment and analysis of damage in l'aquila historic City centre after 6th April 2009. Bull Earthq Eng 9:81–104
- DeJong M (2009) Seismic Assessment Strategies for Masonry Structures (PhD Thesis). Cambridge, Massachusetts, USA: Massachusetts Institute of Technology
- Dolan J (1992) Monotonic and Cyclic nail connection tests. Can J Civ Eng, 19(1)
- EC5 (2004) EN-1995-1-1:2004. Eurocode 5. Design of timber structures. Part 1–1: general rules and rules for buildings. European Committee for Standardization, Brussels, Belgium
- EC6 (2005) EN 1996-1-1. Eurocode 6: design of masonry structures Part 1-1: general rules for reinforced Nd unreinforced masonry structures. European Committee for Standardization, Brussels, Belgium
- Feenstra P, De Borst R (1996) A composite model plasticity for concrete. Int J Solids Struct 33(5):707–730 FEMA 306 (1998) Evaluation of Earthquake-Damaged Concrete and Masonry Wall Buildings. Applied Technology Council (ATC-43 Project)
- FEMA 356 (2000) Prestandard and commentary for the seismic rehabilitation of buildings. American Society of Civil Engineers
- Fiorentino G, Forte A, Pagano E, Sabetta F, Baggio C, Lavorato D, Nuti C, Santini S (2018) Damage patterns in the town of amatrice after August 24th 2016 central Italy earthquakes. Bull Earthq Eng 16:1399–1423
- Griesbach P, Wilson R, Karakus B, Pulatsu B (2024) Transferring Vision-Based data to discontinuum analysis for the assessment of URM walls. Eur J Environ Civil Eng 28(6):1354–1369
- Grünthal G, Musson R, Schwarz J, Stucchi M (1998) European macroseismic scale 1998. Cahiers de Centre Européen de Géodynamique et de Sismologie, Luxembourg
- Grunwald C, Khalil A, Schaufelberger B (2018) Reliability of collapse simulation—Comparing finite and applied element methods at different levels. Eng Struct 176:265–278
- Guerrini G, Salvatori C, Senaldi I, Penna A (2021) Experimental and numerical assessment of seismic retrofit solutions for stone masonry buildings. Geosciences 11(16):230
- Khattak N, Derakhshan H, Thambiratnam D, Malomo D, Perera NJ (2023) Modelling the in-plane/out-ofplane interaction of brick and stone masonry structures using applied element method. J Building Eng 76:107175
- Khorsandnia N, Crews K (2015) Application of Quasi-Brittle material model for analysis of timber members. Australian J Struct Eng 16(2):99–115
- Kita A, Cavalagli N, Masciotta MG, Lourenço PB, Ubertini F (2020) Rapid post-earthquake damage localization and quantification in masonry structures through multidimensional non-linear seismic IDA. Eng Struct 219(10):110841
- Korswagen P, Longo M, Meulman E, Rots J (2019) Crack initiation and propagation in unreinforced masonry specimens subjected to repeated in-plane loading during light damage. Bull Earthq Eng 17:4651–4687
- Korswagen PA, Longo M, Meulman E, Rots J (2020) High resolution monitoring of the initial development of cracks in experimental masonry shear walls and their reproduction in finite element models. Eng Struct 211:110365
- Kouris L, Penna A, Magenes G (2019) Dynamic modification and damage propagation of a Two-Storey Full-Scale masonry Building. Advances in Civil Engineering
- Kouris L, Penna A, Magenes G (2022) Assessment of a Full-Scale unreinforced stone masonry Building tested on Shaking-Table by inverse engineering. Buildings 12(8):1235
- Kuwata Y, Takada S, Bastami M (2005) Building damage and human casualties during the Bam-Iran earh-quake. Asian J Civil Eng (Building Hous 6:1–19
- Livesley R (1992) A computational model for the limit analysis of three-dimensional masonry structures. Meccanica 27:161–172
- Lourenço PB (1996) Computational Strategy for Masonry Structures (PhD Thesis), Delft, Netherlands: Delft University of Technology
- Lourenço PB (2009) Recent advances in masonry modelling: micromodelling and homogenisation. Multiscale modeling in solid mechanics. Computational Approaches
- Magenes G, Penna A, Galasco A, Rota M (2010a) Experimental characterization of stone masonry mechanical properties. Dresden, Germany, 8th International Masonry Conference
- Magenes G, Penna A, Galasco A (2010b) In-plane cyclic shear tests of undressed double-leaf stone masonry panels. Dresden, Germany, 8th International Masonry Conference
- Magenes G, Penna A, Galasco A (2010c) A full-scale shaking table test on a two-storey stone masonry building. Ohrid, Republic of Northern Macedonia, 14th European Conference on Earthquake Engineering
- Magenes G, Penna A, Senaldi I, Rota M, Galasco A (2013) Shaking table test of a strengthened full scale stone masonry Building with flexible diaphragms. Int J Architectural Herit 8(3):349–375



- Malomo D, DeJong M (2022) A Macro-Distinct element model (M-DEM) for simulating the in-plane/out-of-plane interaction and combined failure of unreinforced masonry structures. Earthquake Eng Struct Dynam 51(4):793–811
- Malomo D, Pulatsu B (2024) Discontinuum models for the structural and seismic assessment of unreinforced masonry structures: a critical appraisal. Structures 62:106108
- Malomo D, Pinho R, Penna A (2018) Using the applied element method for modelling calcium silicate brick masonry subjected to in-plane Cyclic loading. Earthquake Eng Struct Dynam 47(7):1610–1630
- Malomo D, Pinho R, Penna A (2019) Applied element modelling of the dynamic response of a Full-Scale clay brick masonry Building specimen with flexible diaphragms. Int J Architectural Herit 14(10):1484–1501
- Meguro K, Tagel-Din H (1997) A new efficient technique for fracture analysis of structures. Bull Earthq Resistant Struct 30:103–116
- Meguro K, Tagel-Din H (1999) Simulation of buckling and post-buckling behavior of structures using applied element method. Bull Earthq Resistant Struct 32:125–135
- Meguro K, Tagel-Din H (2000) Applied element method for structural analysis: theory and application for linear materials. JSCE Struct Eng Earthq Eng 17:21–35
- Milani G, Esquivel YW, Lourenço PB, Riveiro B, Oliveira DV (2013) Characterization of the response of quasi-periodic masonry: geometrical investigation, homogenization and application to the Guimarães castle. Portugal Eng Struct 56:621–641
- Morandini C (2022) Integrated Nonlinear Modelling Strategies for the Seismic Analysis of Masonry Structures (PhD Thesis). University of Pavia, Pavia, Italy
- Parisi F, Augenti N (2013) Seismic capacity of irregular unreinforced masonry walls with openings. Earth-quake Eng Struct Dynam 42:101–121
- Parisi F, Balestrieri C, Varum H (2019) Nonlinear finite element model for traditional Adobe masonry. Constr Build Mater 233:450–462
- Pulatsu B (2023) Coupled elasto-softening contact models in DEM to predict the in-plane response of masonry walls. Comput Part Mech 10:1759–1770
- Pulatsu B, Erdogmus E, Lourenço PB, Quey R (2019) Simulation of uniaxial tensile behavior of quasi-brittle materials using softening contact models in DEM. Int J Fract 217:105–129
- Pulatsu B, Erdogmus E, Lourenço PB, Lemos JV, Tuncay K (2020) Simulation of the in-plane structural behavior of unreinforced masonry walls and buildings using DEM. Structures 27:2274–2287
- Pulatsu B, Gonen S, Parisi F, Erdogmus E, Tuncay K, Funari M, Lourenco PB (2022) Probabilistic approach to assess URM walls with openings using discrete rigid block analysis (D-RBA). J Building Eng 61:105269
- Pulatsu B, Gonen S, Funari M, Parisi F (2023a) Spatial stochastic D-RBA and limit equilibrium analysis of unreinforced masonry pier-spandrel structures. Eng Struct 296:116897
- Pulatsu B, Gonen S, Parisi F (2023b) Effect of precompression and material uncertainty on the In-Plane behavior of URM Pier-Spandrel system. Buildings 13(1):203
- Quagliarini E, Maracchini G, Clementi F (2017) Uses and limits of the equivalent frame model on existing unreinforced masonry buildings for assessing their seismic risk: A review. J Building Eng 10:166–182
- Reagan D, Sabato A, Niezrecki C (2018) Feasibility of using digital image correlation for unmanned aerial vehicle structural health monitoring of bridges. Struct Health Monit 17(5):1056–1072
- Rezaie A, Godio M, Beyer K (2021) Investigating the cracking of plastered stone masonry walls under shear-compression loading. Constr Build Mater 306:124831
- Sarhosis V, Dais D, Smyrou E, Bal IE, Droukgas A (2021) Quantification of damage evolution in masonry walls subjected to induced seismicity. Eng Struct 243:112529
- Silva L, Lourenço PB, Milani G (2020) Numerical homogeneization-based seismic assessment of an Englishbond masonry prototype: structural level application. Earthquake Eng Struct Dynam 49(9):841–862
- Szabò S, Funari MF, Lourenço PB (2023) Masonry patterns' influence on the damage assessment of URM walls: current and future trends. Developments Built Environ 100:100–119
- TNO DIANA (2009) DIANA, displacement method analyser, release 9.4, user's manual. TNO DIANA, Delft, The Netherlands
- Tomassetti U, Correia A, Graziotti F, Penna A (2019) Seismic vulnerability of roof systems combining URM gable walls and timber diaphragms. Earthquake Eng Struct Dynam 48(11):1297–1318
- Tomić I, Vanin F, Boćulic I, Beyer K (2021) Numerical simulation of unreinforced masonry buildings with timber diaphragms. Buildings 11(5):205
- Van Der Plujm R (1993) Shear behaviour of bed joints. Philadelphia, USA, Proceedings of the 6th North American Masonry Conference

Publisher's note Springer Nature remains neutral with regard to jurisdictional claims in published maps and institutional affiliations.

